ORIGINAL ARTICLE

Modification of the isotopic and geochemical compositions of accessory minerals controlled by microstructural setting

Chris Clark[1] | Richard J. M. Taylor[1,2] | Malcolm P. Roberts[3] | Simon L. Harley[4]

[1]The Institute for Geoscience Research (TIGeR), School of Earth and Planetary Sciences, Curtin University, Perth, Australia

[2]Carl Zeiss Microscopy Ltd, Cambridge, UK

[3]Centre for Microscopy, Characterisation and Analysis, University of Western Australia, Perth, Australia

[4]School of Geociences, University of Edinburgh, Edinburgh, UK

Correspondence
Prof Chris Clark, School of Earth and Planetary Sciences, Curtin University, Perth, Western Australia 5102, Australia.
Email: c.clark@curtin.edu.au

Abstract

In situ age and trace element determinations of monazite, rutile and zircon grains from an ultrahigh temperature (UHT) metapelite-hosted leucosome from the Napier Complex using laser split-stream analysis reveal highly variable behaviour in both the U–Pb and trace element systematics that can be directly linked to the microstructural setting of individual grains. Monazite grains armoured by garnet and quartz retain two concordant ages 2.48 and 2.43 Ga that are consistent with the previously determined ages for peak UHT metamorphism in the Napier Complex. Yttrium in the armoured grains is unzoned with contents of ∼700 ppm for the garnet-hosted monazite and in the range 400–1,600 ppm for the monazite enclosed within quartz. A monazite grain hosted within mesoperthite records a spread of ages from 2.43 to 2.20 Ga and Y contents ranging between 400 and 1,700 ppm. This grain exhibits core to rim zoning in both Y and age, with the cores enriched in Y relative to the rim and younger ages in the core relative to the rim. A monazite grain that sits on a grain boundary between mesoperthite and garnet records the largest spread in ages—from 2.42 to 2.05 Ga. The youngest ages in this grain are within a linear feature that reaches the core and is connected to the grain boundary between the garnet and mesoperthite; the oldest ages are observed where monazite is in contact with garnet. Yttrium in the grain is enriched in the core and depleted at the rim with the strongest depletions where monazite is adjacent to grain boundaries between the silicate minerals or in contact with garnet. The unarmoured monazite grains have lower intercept ages of 1.85 Ga, which overlaps with the bulk of ages determined from the rutile and is coincident with a previously reported zircon age obtained through depth profiling from the Napier Complex. The age and chemical relationships outlined above illustrate decoupling between the geochemical and geochronological systems in monazite. Individual grains are suggestive of a range of processes that modify these systems, including volume diffusion, flux-limited diffusion and fluid-enhanced recrystallization, all operating at the scale of a single thin section and primarily controlled by host mineral microstructural

setting. These findings illustrate how the development of simple partitioning coefficients (cf. garnet/zircon) and geospeedometry based on experimentally determined diffusion coefficients on grain separates may not be achievable. However, it highlights the utility of combining age and trace element concentrations from multiple accessory minerals with microstructural information when trying to build a complete history of tectonothermal events experienced by an ancient rock system that has undergone a prolonged history of thermal, deformational and fluid flow events.

1 | INTRODUCTION

The mineral monazite is thought to be a robust recorder of the timing of high to ultrahigh temperature (UHT) metamorphic events (Dumond et al., 2015; Holder et al., 2018; Korhonen et al., 2013) as studies on Pb diffusion have shown it to have limited diffusive length scales at temperatures and durations comparable to those determined for orogenic events (Cherniak et al., 2004; Cherniak & Pyle, 2008). In addition, the chemistry of monazite has been interpreted to record the growth/breakdown of major silicate minerals potentially allowing the direct linking of age to pressure and temperature information (Foster et al., 2002; Hermann & Rubatto, 2003; Holder et al., 2015; Mottram et al., 2014; Rubatto et al., 2013) with some studies beginning to develop a systematic framework for the partitioning of Y and HREE between monazite and garnet in response to changing pressures and temperatures (Buick et al., 2006; Warren et al., 2019). The interpretations and applications of these empirical relationships and their extrapolation to higher temperatures require the isotopic and elemental geochemical systems within monazite remain fully coupled during the protracted high-temperature evolutions recorded by lower crustal rocks. However, there is a growing body of evidence that presents a strong case for microscale to nanoscale intragrain Pb-mobility during metamorphism (Seydoux-Guillaume et al., 2019, 2003; Turuani et al., 2022, 2023), which can be enhanced by deformation (Erickson et al., 2015; Fougerouse et al., 2018) and/or in the presence of fluids or melt (Grand'Homme et al., 2016; Varga et al., 2020; Weinberg et al., 2020; Williams et al., 2011). In many cases, evidence for the infiltration of a fluid is cryptic as the silicate assemblage may show little sign of alteration, therefore a mineral like monazite that is reactive in the presence of fluids and is able to record thermal/fluid infiltration events that leave no pervasive imprint on the rock (Taylor et al., 2014). The reactivity of monazite is particularly useful in terranes that have previously undergone high-temperature events that have dehydrated the system leaving them unreactive in terms of major mineral assemblages in the event that they experience a subsequent thermal event associated with limited volumes of hydrous fluid infiltration.

To investigate whether the residence of a rock at high-temperatures has a measurable impact on the geochemical characteristics of monazite, we examined the U–Pb and trace and rare earth element systematics of monazite grains from a UHT granulite facies metapelite from the Napier Complex in East Antarctica. The individual monazite grains were 'mapped' with laser-ablation split steam analyses in an individual thin-section, thus preserving the 2D microstructural context of the grains and their relationships to grain boundaries and host minerals (Kylander-Clark et al., 2013). This approach also enables direct comparison of both the isotopic age data and the geochemical data as they are collected from the same analytical volume (Weller et al., 2020). In addition, to provide further geochronological context for the sample, we collected LASS datasets from rutile and zircon grains from within the sample as well as electron probe maps of rutile. These datasets allow the development of a robust temporal framework within which the monazite dataset may be interpreted.

2 | GEOLOGICAL SETTING AND SAMPLE DETAILS

The Napier Complex consists of poly-deformed and potentially poly-metamorphosed Archaean rocks that crop out along the coast, islands and mountain ranges of Enderby Land in East Antarctica (Figure 1). The Napier Complex is characterized by the regional occurrence of UHT mineral assemblages with corresponding peak metamorphic conditions of temperatures of 1,050–1,120°C and pressures of 0.7–1.1 GPa. The highest
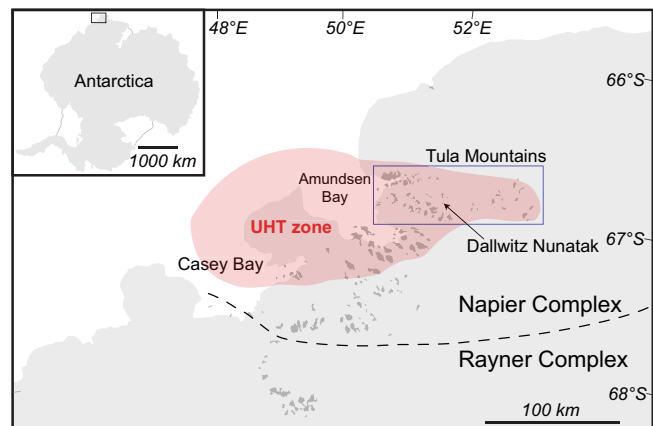
FIGURE 1 Map of the Napier Complex in East Antarctica highlighting the area of UHT metamorphism, the location of Amundsen Bay and the Tula Mountains and Dallwitz Nunatak—the sample location in this study.

temperatures in the Napier Complex are restricted to a central part of the Napier Complex with the metamorphic isograds decreasing in grade away from this area (Harley & Black, 1997; Harley & Hensen, 1990; Hokada et al., 2008; Kelly & Harley, 2005; Sheraton et al., 1987).

The timing of metamorphism and deformation within the Napier Complex has been and continues to be the subject of ongoing debate. However, recent studies have found abundant evidence of metamorphic zircon growth in the age range 2580–2450 Ma coupled with Ti-in-zircon thermometry from the grains that record temperatures >900°C suggesting that peak UHT metamorphism occurred at this time and persisted for >130 Myr (Clark et al., 2018; Harley, 2016).

2.1 | Sample and microstructural position of monazite grains

The analysed monazite grains occur in Sample 11178/4 from Dallwitz Nunatak in the Tula Mountains of the Napier Complex (Figure 1). This is a sample of a metapelitic migmatite consisting of residual domains of garnet-sillimanite-spinel-quartz with accessory rutile and zircon (Figure 2a) and leucosome dominated by quartz and mesoperthite with rare garnet grains and accessory rutile, monazite and zircon (Figure 2a). The P–T conditions for this sample are inferred to be similar to those reported from other locations within the Tula Mountains where the common occurrences of osumillite + sapphirine + quartz in Mg-metapelites are indicative of temperatures in excess of 1,000°C at pressures of 7–8 kbar (Ellis, 1980; Harley & Motoyoshi, 2000). Dallwitz Nunatak, originally referred to as Spot height 945, was the location where

sapphirine + quartz, a diagnostic UHT mineral assemblage, was first identified (Dallwitz, 1968).

Leucosome-hosted monazite grains from four microstructural settings were chosen for laser ablation split stream (LASS) analysis whereby both age and geochemical information were collected simultaneously. The first grain (Mnz1), located at the junction of three grain boundaries between a garnet and two mesoperthite grains (Figure 2b), is subhedral and ∼250 μm in diameter. A second monazite grain (Mnz2) with a diameter of ∼150 μm is entirely armoured by garnet and separated from Mnz1 by ∼100 μm of garnet (Figure 2b). The third analysed monazite (Mnz3) occurs at the junction of four mesoperthite grains and proximal to two euhedral garnet grains (Figure 2c). The final monazite grain analysed (Mnz4), at ∼100 μm in diameter the smallest of the grains, is enclosed within a quartz grain that contains crystallographically controlled exsolved rutile needles (Figure 2d). All zircon, rutile and garnet data were collected in situ, and the analysed grains are indicated in Figures 2a–e.

3 | METHODS

3.1 | Monazite laser ablation split stream

Collection of LA–(MC)–ICP–MS data was performed at the GeoHistory Facility in the John de Laeter Centre, Curtin University, Perth, Australia. Individual monazite grains were ablated using an ASI RESOlution M-50A-LR, incorporating a Compex 193 nm Ar-F excimer laser attached in split stream (LASS) mode (Kylander-Clark et al., 2013) to a Nu Instruments Nu-Plasma2 HR multi-collector ICP-MS and Agilent 7700 quadrupole ICP-MS. All data are reported in Table S1.

The Nu-Plasma2 was set up to collect U and Th on faraday cups, whilst all Pb and Hg peaks were measured using high sensitivity ion counters. Analyses were performed at a laser repetition rate of 6 Hz and a 7 μm spot diameter at 26% attenuation, resulting in a power output of ∼2 J/cm² at the sample surface. A single analysis involved two cleaning pulses, a long initial background collection of 40 s, followed by 25 s of ablation and 15 s of washout time. A long background collection on the highly sensitive ion counters is essential for the use of the 'step forward' baseline collection on the Iolite software. Laser gas flows of 320 ml/min He and 1.2 ml/min N were used, with matched mass spec argon gas flows of ∼1 L/min on the Nu Plasma2 and ∼1 L/min on the Agilent. The following elements were monitored for 0.03 s each: ^{28}Si, ^{31}P, ^{34}S, ^{44}Ca, ^{88}Sr, ^{89}Y, ^{139}La, ^{140}Ce, ^{141}Pr, ^{146}Nd, ^{147}Sm, ^{151}Eu, ^{157}Gd, ^{159}Tb, ^{163}Dy, ^{165}Ho, ^{166}Er, ^{168}Tm, ^{172}Yb, ^{175}Lu, ^{178}Hf, ^{232}Th, ^{238}U.
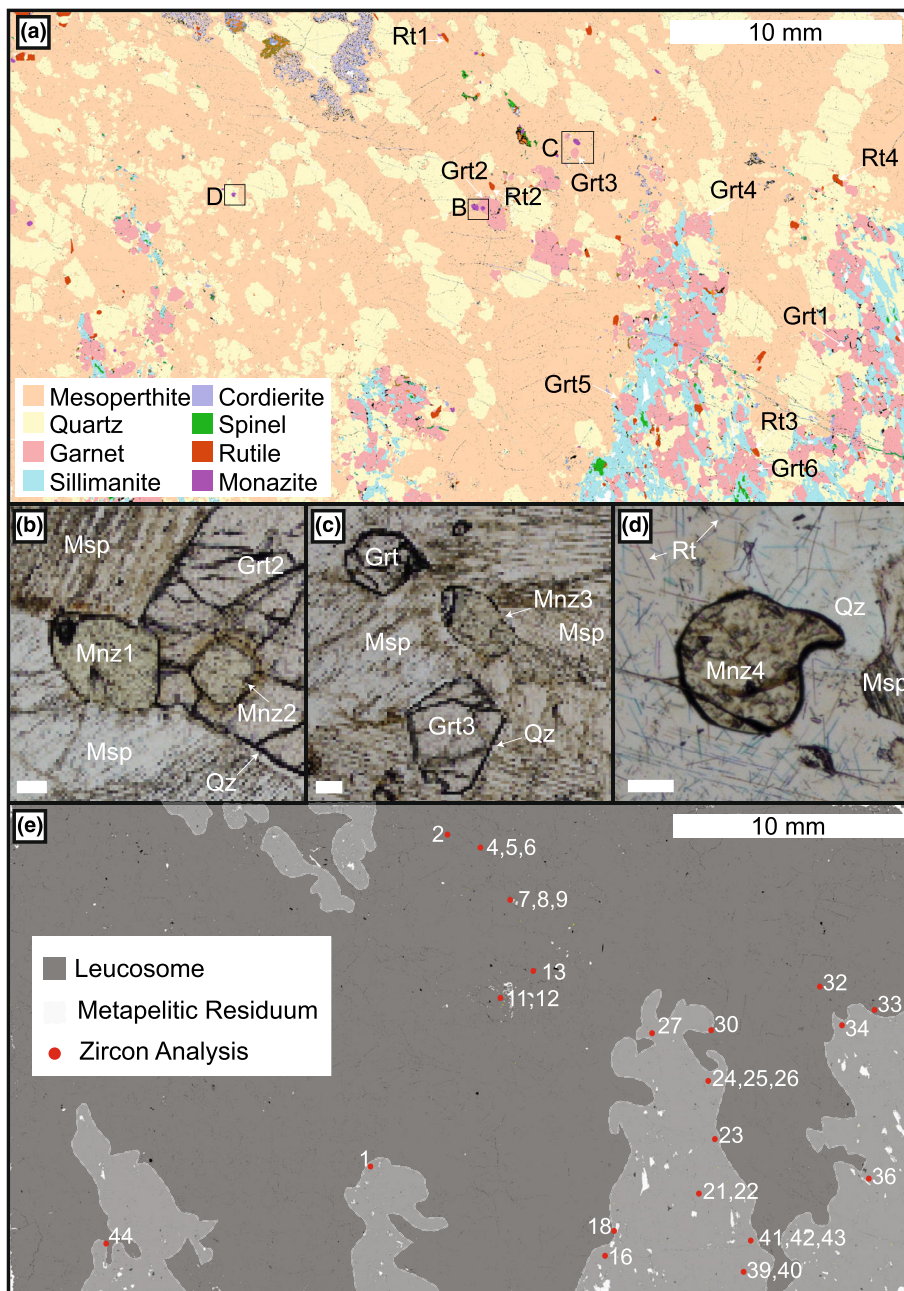
FIGURE 2 (a) Tescan integrated mineral analyser (TIMA) map of Sample 11178/4 illustrating the distribution of minerals within the sample. Locations of individual grains analysed in this study are labelled. (b) Plane-polarized light image of Mnz1 and Mnz2 highlighting the petrographic relationships between monazite grains and the garnet and the leuscosome minerals. (c) Plane-polarized light image of the location of Mnz3 at the junction of grain boundaries within the leucosome and the proximity to leuscomse hosted garnet. (d) Plane-polarized light image of Mnz4, which is enclosed within a rutilated quartz grain. (e) BSE image highlighting the distribution of leucosome and metapelitic residuum and the distribution of the zircon grains analysed in this study. All mineral abbreviations after Whitney and Evans (2010) except for mesoperthite (Msp). Scale bars in (b), (c) and (d) are all 50 μm.

The time-resolved mass spectra for monazite were reduced using the U_Pb_Geochronology4 data reduction scheme in Iolite (Paton et al., 2011). The primary reference material used in this study was 44,069 (424.9 ± 0.4 Ma; Aleinikoff et al., 2006) with Curtin University standard India (509 Ma: this study 511 ± 3 Ma; Korhonen et al., 2011; Taylor et al., 2014) used as a secondary age standard. $^{206}Pb/^{238}U$ ages calculated for secondary monazite age standard analyses were used to calculate an additional uncertainty required for a single analytical population in this material. This additional uncertainty of ~1% was subsequently added to the $^{206}Pb/^{238}U$ ages of the unknowns. For the calculation of other weighted means and the plotting of concordia diagrams, an additional uncertainty of 0.8% was added to the analytical uncertainties for the $^{207}Pb/^{235}U$ and $^{207}Pb/^{206}Pb$ ratios.

Monazite trace element analyses were processed using the methodology of Clark et al. (2019). This involves internally standardizing using Ce by calibrating the trace element data against multiple standards of known Ce concentrations covering a broad range of values. This enables the production of a working curve for each analytical session of Ce concentration against counts per second (CPS) on the quadrupole. This is then used to calibrate each unknown for its individual Ce concentration based on CPS using the TraceElements_SI DRS function in Iolite. As these data are collected during the run itself, this approach is time and cost effective,

with the added benefit that the calibration uses an identical sample volume as the measurement of the unknown. Multiple EPMA measurements for five monazite standards gave the following Ce concentrations used for calibration: 44,069 = 23.3 wt%, GM3 = 22.3 wt %, Khan = 29.0 wt%, Farm Eureka = 29.2 wt%, India = 19.9 wt%. These standards show an ∼10% variation in total Ce variation, covering the majority of monazite compositions, and provide a robust Ce calibration for the unknowns. The calibrated results for the unknowns in this study showed a variation in Ce of 22–31 wt%. The REE values were normalized to chondritic values (Anders & Grevesse, 1989).

3.2 | Rutile: LASS-EPMA maps

Rutile analyses were collected using an ASI RESOlution M-50A-LR, incorporating a Compex 193 nm Ar-F excimer laser attached to a Nu-Plasma2 HR multi-collector ICP and Agilent 8900 triple quadrupole ICP to enable simultaneous in situ U–Pb and trace-element collection. All data are reported in Table S2. The Nu-Plasma2 was set up to collect U and Th on Faraday cups, whilst all Pb and Hg peaks were measured using high sensitivity ion counters. The Agilent 8900 quadrupole was set up to monitor trace elements for 0.03 s; ^{24}Mg, ^{27}Al, ^{29}Si, ^{44}Ca, ^{45}Sc, ^{49}Ti, ^{51}V, ^{52}Cr. ^{57}Fe, ^{60}Ni, ^{63}Cu, ^{66}Zn, ^{89}Y, ^{90}Zr, ^{93}Nb, ^{95}Mo, ^{118}Sn, ^{121}Sb, ^{178}Hf, ^{181}Ta, ^{182}W, ^{204}Pb, ^{206}Pb, ^{207}Pb, ^{208}Pb, ^{232}Th, ^{238}U.

The laser employed a repetition rate of 4 Hz at a 50 μm spot size and at a 26% beam attenuation leading to a fluence of ∼2 J/cm^2. Each analysis consisted of two cleaning pulses, a background of 40 s, followed by 35 s of ablation and 15 s of washout time. Laser gas flows of 320 ml/min He and 1.2 ml/min N were mixed with an argon gas flow of ∼1 L/min on both the Nu Plasma II and Agilent 8900 QQQ. Reference materials for rutile consisted R10 (1,090 Ma; Luvizotto et al., 2009), R19 (489.5 ± 0.9 Ma; Zack et al., 2011) and secondary RMs—BCR, BHVO (Jochum et al., 2005) and TIG (Jochum et al., 2011)—were inserted into the run, bracketing every 15 unknowns.

Data were processed in *Iolite v3*; U–Pb data were reduced with the U_Pb_Geochronology4 data reduction scheme following Paton et al. (2011), using R10 as the primary RM. Secondary RM R19 yielded ^{206}Pb/^{238}U ages within 2.39% of its accepted values. Trace-element calibration was conducted using ^{47}Ti as the internal standard, assuming 59.94 wt% and BHVO (^{24}Mg, ^{27}Al, ^{28}Si, ^{44}Ca, ^{45}Sc, ^{52}Cr. ^{57}Fe, ^{60}Ni, ^{63}Cu, ^{66}Zn, ^{89}Y, ^{118}Sn, ^{232}Th) and R10 (^{49}Ti, ^{51}V, ^{90}Zr, ^{93}Nb, ^{95}Mo, ^{121}Sb, ^{178}Hf, ^{181}Ta, ^{182}W, ^{204}Pb, ^{206}Pb, ^{207}Pb, ^{208}Pb, ^{238}U) were used as the primary

RMs using the TraceElements data reduction scheme within Iolite. Zirconium content within rutile was used for the temperature calculation following the calibration of Tomkins et al. (2007) at pressures of 8 kbars.

Element maps were acquired on the JEOL JXA8530F hyperprobe equipped with five tuneable wavelength dispersive spectrometers at the Centre for Microscopy, Characterisation and Analysis University of Western Australia. Operating conditions were a beam energy of 25 keV and a beam current of 100 nA for instrument calibration. Elements reported here, Zr, Al, Ti, Mn, Ni, Nb, Si, V, Fe and Hf, were analysed using PetJ, TAP, LiFH and LiF crystals and a suite of proprietary metals, oxides, silicates and phosphates standards for instrument calibration. Mean atomic number (MAN) background correction was used throughout (Donovan & Tingle, 1996) and unknown and standard intensities were corrected for deadtime. Interference corrections were applied as appropriate using the method of Donovan et al. (1993). The quantitative map acquisition was performed using the Probe Image® software for X-ray intensity acquisition. The beam current used for mapping was 200 nA with a 150 ms per pixel dwell time and a 1 × 1 pixel dimension. Image processing and quantification were performed off-line with the CalcImage® software and output to Surfer® for further handling and presentation.

3.3 | Zircon LASS

Collection of LA–ICP–MS data was performed at the GeoHistory Facility in the John de Laeter Centre, Curtin University, Perth, Australia. Individual zircon grains were ablated using an ASI RESOlution M-50A-LR, incorporating a Compex 193 nm Ar-F excimer laser attached in split stream (LASS) mode (Kylander-Clark et al., 2013) to a Nu Instruments Nu-Plasma2 HR multi-collector ICP-MS and Agilent 7700 quadrupole ICP-MS. All data are reported in Table S3. The Nu-Plasma2 was set up to collect U and Th on faraday cups, whilst all Pb and Hg peaks were measured using high sensitivity ion counters. The Agilent quadrupole was set up to collect the following trace elements, each of which were monitored for 0.03 s: ^{29}Si, ^{31}P, ^{49}Ti, ^{89}Y, ^{90}Zr, ^{93}Nb, ^{147}Sm, ^{151}Eu, ^{157}Gd, ^{159}Tb, ^{163}Dy, ^{165}Ho, ^{166}Er, ^{168}Tm, ^{172}Yb, ^{175}Lu, ^{178}Hf, ^{204}Pb, ^{232}Th, ^{238}U. Analyses were performed at a laser repetition rate of 6 Hz and a 23 μm spot diameter at 26% attenuation, resulting in a power output of ∼2 J/cm^2 at the sample surface. A single analysis involved two cleaning pulses, a long initial background collection of 40 s, followed by 25 s of ablation and 15 s of washout time. A long background collection on the highly sensitive ion counters is essential for the use of the 'step forward'

baseline collection on the Iolite software. Laser gas flows of 320 ml/min He and 1.2 ml/min N were used, with matched mass spec argon gas flows of ∼1 L/min on the Nu Plasma2 and ∼1 L/min on the Agilent.

The time-resolved mass spectra were reduced using the U_Pb_Geochronology4 data reduction scheme in Iolite (Paton et al., 2011). The primary reference material used in this study was 91,500 (1062.4 ± 0.4 Ma; Wiedenbeck et al., 1995) with Plesovice (337.1 ± 0.4 Ma; Sláma et al., 2008), GJ1 (601.9 ± 0.7 Ma; Jackson et al., 2004) and Curtin University internal standard KLDF (553.3 ± 0.3 Ma) used as secondary age standards. $^{206}Pb/^{238}U$ ages calculated for the secondary zircon age standards were used to calculate an additional uncertainty required for a single analytical population in these materials. This additional uncertainty of ∼1% was incorporated into the calculation of the $^{206}Pb/^{238}U$ age of the unknowns. For the calculation of other weighted means and the plotting of concordia diagrams, an additional 0.5% uncertainty was added to the analytical uncertainties for the $^{207}Pb/^{235}U$ and $^{207}Pb/^{206}Pb$ ratios. Internal standardization for trace elements used a stoichiometric Zr concentration of 49.7% in zircon standard GJ-1 (Jackson et al., 2004).

The titanium content of zircon coexisting with rutile and quartz has a strong dependence on temperature, and this dependence has been calibrated as a thermometer (Watson & Harrison, 2005) and applied to UHT rocks (e.g., Baldwin et al., 2007; Korhonen et al., 2014; Shaffer et al., 2017). We have applied this thermometer to the metamorphic zircon grains using the calibration for Ti-in-zircon of Ferry and Watson (2007). An assumption of unity for all activities of SiO_2, TiO_2 and ZrO_2 is made as the rock contains abundant quartz, rutile and zircon. For Ti-in-zircon thermometry, rather than simply taking the highest temperature determined from the dataset, we follow the proposal by Tomkins et al. (2007) and use a conservative estimate of temperature as given by the upper bound of a box-plot box. These authors suggested the uncertainty associated with this value be approximated as ±30°C or half the interquartile range if this is larger, based on the rationale that the real uncertainty relates to the scatter in the data rather than to analytical uncertainties combined with calibration uncertainties, which are likely to be much smaller than ±30°C.

3.4 | Garnet LA-ICPMS

Rare earth element and other trace element compositions of garnet were measured by LA–ICP–MS using an ASI RESOlution M-50A-LR, incorporating a Compex 193 nm Ar-F excimer laser with an Agilent 8900 mass spectrometer at Curtin University. Garnet grains were analysed in a polished thin section using a 50 μm spot size and an ablation period of 30 s with a repetition rate of 7 Hz. NIST glasses (610, 612) (Pearce et al., 1997) were used as reference materials, with NIST 610 as the primary standard. Calibration of trace elements in garnet assumed stoichiometric Si (18 wt%). Time-resolved data were processed following each session using the Iolite software (Paton et al., 2011, 2010), which permits detection of data affected by analysing inclusions. All data are reported in Table S4.

4 | RESULTS

4.1 | Monazite

4.1.1 | Monazite Grain 1 (Mnz1)

The $^{207}Pb–^{206}Pb$ ages from Mnz1 range from 2421 ± 29 Ma to 2033 ± 14 Ma with individual analyses becoming more discordant with decreasing age (Figure 3a). The Y content of the grain Mnz1 ranges from 1,370 to 134 ppm (Figure 3b); there is a weak correlation when Y content is plotted against $^{207}Pb–^{206}Pb$ age (Figure 3b). A linear increase in U is evident when plotted against Y (Figure 3c). The Th content is relatively constant for Y concentrations between 700 and 1,500 ppm but is highly variable for Y contents below 700 ppm ranging from 2% to 6 wt% (Figure 3d). The age and elemental maps for Mnz1 show that there is a younger age domain that runs from the upper righthand side, where the grain abuts the garnet and mesoperthite grains, towards the core of the grain (Figures 2b and 4b). The oldest ages are located where the grain in is contact with the neighbouring garnet grain (Figure 4b). The Y map of grain Mnz1 highlights a core with high Y, overlapping with but offset from the low apparent age domain, and the lowest Y areas occurring at the margins of the grain particularly where the grain is in contact with either two other grains or garnet (Figures 2b and 4c). A chondrite normalized REE plot coloured for $^{207}Pb–^{206}Pb$ age reveals a systematic decrease in the abundance of M-HREE with decreasing apparent age, along with a decrease in the absolute Eu content and a more pronounced Europium anomaly (Eu*/Eu; where Eu* = 0.5*[Sm + Gd]; Figure 5a). A bivariate plot of Gd against Y (Figure 6a) illustrates how the two elements are strongly correlated, when the distribution of Gd within Mnz1 is plotted as a map the Y and Gd concentrations are spatially well correlated, the highest concentrations being observed in the core and systematically decreasing rimwards. As was seen in the Y map (Figure 4c), Gd is most depleted where the monazite grain abuts grain boundaries (Figure 6a). Conversely, there is a subtle near-rim
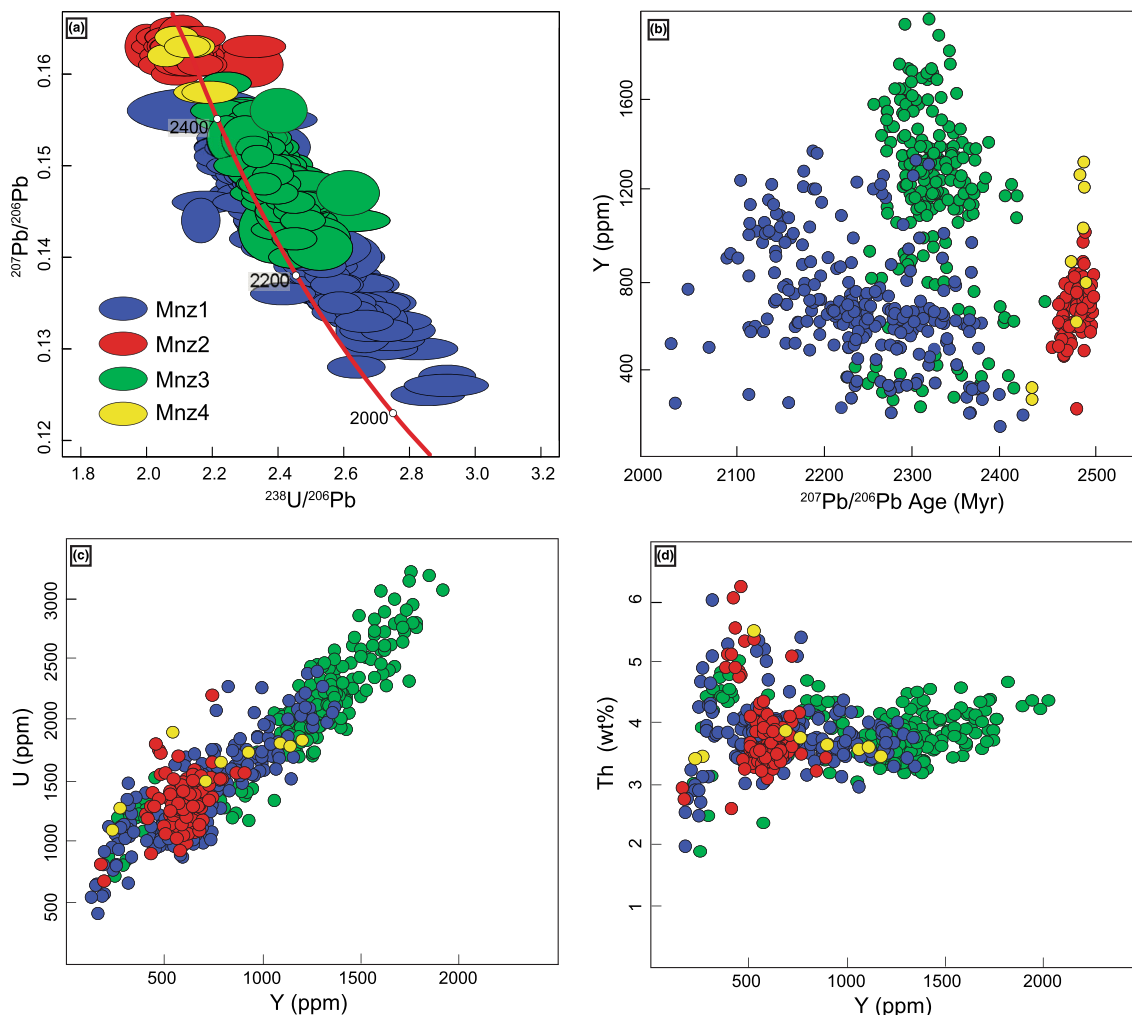
—WILEY—|

FIGURE 3 Laser ablation split stream monazite data (a) Tera-Wasserburg concordia diagram, colour coded by individual grain. (b) Yttrium versus ^{207}Pb/^{206}Pb age diagram. (c) Uranium versus yttrium diagram. (d) Thorium versus yttrium diagram.

enrichment in Nd, as illustrated in the bivariate plot where Y and Nd are moderately anti-correlated and on the map show a slightly higher average Nd towards the edge of the grain (Figure 6b).

4.1.2 | Monazite Grain 2 (Mnz2)

The second analysed grain, Mnz2, is enclosed within a garnet grain and displays very little variation in either age or Y content (Figure 3a,b). The ^{207}Pb–^{206}Pb ages range from 2504 ± 16 to 2454 ± 16 Ma and define a weighted mean age of 2483 ± 1 Ma ($n = 123$, MSWD = 0.42) (Figure 3a). The Y content of Mnz2 ranges from 175 to 900 ppm with the majority of analyses falling between 500 and 800 ppm (Figure 3b). Figure 3c shows that the grain lies on the U-Y correlation trend defined by the other studied monazites but has too small a spread in Y to define that correlation itself. There is no correlation of

Th with Y content of the grain (Figure 3d). The age and Y maps of Mnz2 show very little systematic variation, with no discernable core to rim zoning patterns evident (Figures 4b,c). The chondrite normalized REE plot again shows a broad correlation of HREE abundance with ^{207}Pb–^{206}Pb age; however, there appears to be no strong relationship between Eu anomaly and age in this grain.

4.1.3 | Monazite Grain 3 (Mnz3)

Grain Mnz3 is hosted within mesoperthite grains. It has a broad range in ^{207}Pb–^{206}Pb ages, with a maximum age of 2445 ± 16 Ma and a minimum age of 2227 ± 16 Ma and discordance decreasing with age (Figure 3a). The Y content of Mnz3 has a dominant cluster at around 1,000–1,800 ppm but is variable with a number of analyses yielding concentrations down to 200 ppm (Figure 3b). Mnz3 shows a similar relationship between U and Th to
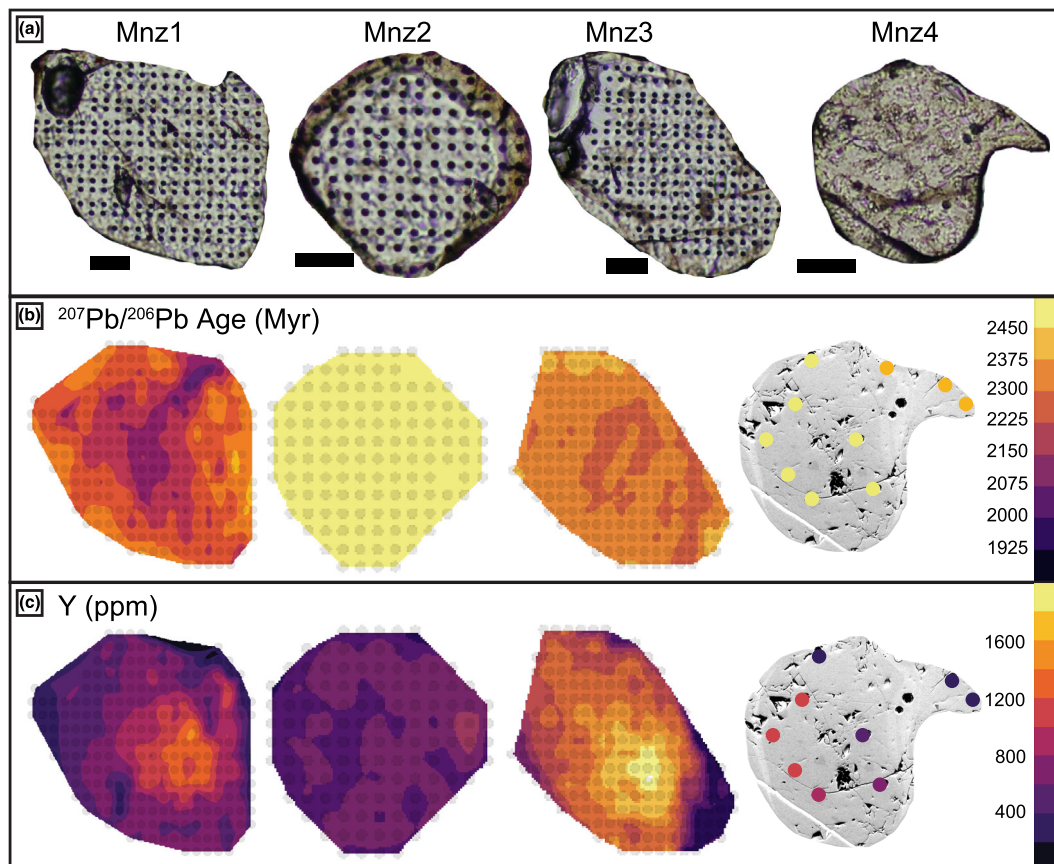
FIGURE 4 (a) Plane-polarized light image of monazite grains analysed in this study showing the location of the individual spots. (b) $^{207}Pb/^{206}Pb$ age maps of grains Mnz1, Mnz2 and Mnz3 and a BSE image of Mnz4 with ages marked. (c) Yttrium maps of grains Mnz1, Mnz2 and Mnz3 and a BSE image of Mnz4 with ages marked. Scale bar is 50 μm.

Y to Mnz1 with U and Y varying together and all but the lowest values of Y having similar Th contents (Figure 3c,d). When the age information is viewed spatially, the younger ages cluster in the core of the grain and two older zones are observed at the tips of the grain (Figure 4b). By contrast, the Y content displays an enriched core with variable degrees of depletion around the margins of the grain (Figure 4c). This distribution is similar to Gd which co-varies with Y (Figure 6a) and shows a strong depletion at the tip of the monazite where it is adjacent to a grain boundary (Figure 2d). The chondrite normalized REE plot shows a decrease in HREE and a more strongly developed negative Eu anomaly for the younger analyses (Figure 5c). By contrast, the reverse is observed for Ce, Pr and Nd, which are relatively enriched in the monazite analyses with younger ages relative to those with older ages (Figure 5c). This relationship can also be seen in the spatially distributed Nd data for this grain, in which the lowermost tip of the grain is relatively enriched in Nd (Figure 6b) where the older ages are recorded.

4.1.4 | Monazite Grain 4 (Mnz4)

The final analysed grain, Mnz4, is armoured entirely within a quartz grain (Figure 2d). As only nine analyses were made within this grain, no age or Y mapping was attempted. A backscattered electron (BSE) image of the grain reveals two domains: a low-response core enclosed by a higher-response protuberance or edge. The two distinct clusters of ages observed on the concordia diagram (Figure 3a) correlate with these domains. The low-response core returns a weighted mean ^{207}Pb–^{206}Pb age of 2487 ± 6 Ma (MSWD 0.12, $n = 7$; Figure 4b), whilst two spot ages from the high-response protuberance were 2434 and 2433 Ma (Figure 4c). The Y content of the low-response monazite is in the range 540–1,190 ppm, whereas the higher-response monazite analyses have 237 and 233 ppm Y. Whilst there are fewer analyses for Mnz4, U contents lie on the U-Y correlation trend defined by the other monazties and the younger, low-Y, Mnz4 protuberance also has lower U contents (Figure 3b,c). Th contents do not correlate with either
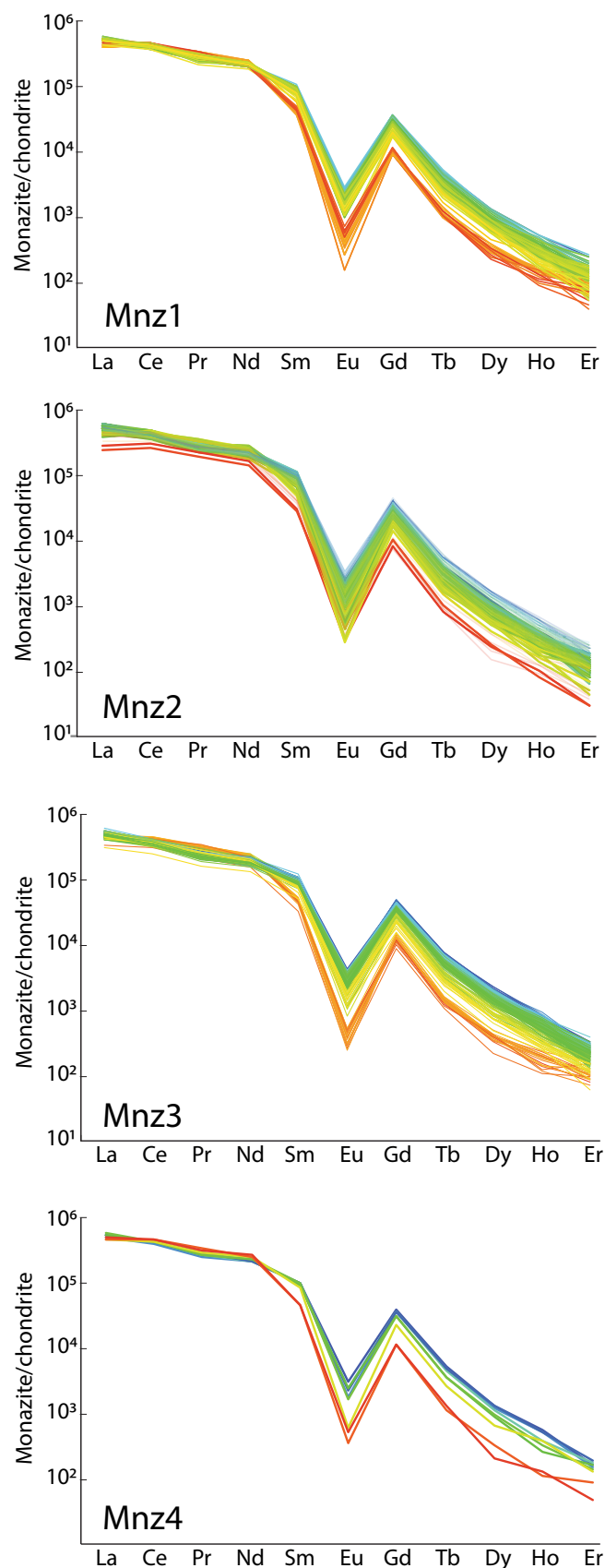
FIGURE 5 Chondrite-normalized REE diagram for grains Mnz1, Mnz2, Mnz3 and Mnz4. Colour coding for grains as per Figure 3.

age or Y (Figure 3d). The chondrite normalized REE plot highlights the two groups of analyses that correlated with their textural position (Figure 5d). The older, lower BSE response monazite analyses have higher relative HREE abundances and less well-developed negative Eu anomalies than the LREE enriched, younger analyses from the higher BSE response protuberance (Figure 5d).

4.2 | Rutile

4.2.1 | Rutile Grain 1 (Rt1)

Rt1 is located within the leucosome (Figure 2a) and is in contact with mesoperthite grains, a monazite grain and a zircon grain (Figure 7a). The BSE response of the grain is uniform throughout the grain as are the Ti, Zr and Si elemental maps (Figure 7e,i,m). An inclusion of an Al and Si rich phase is observed in the lower right of the grain at the junction between grain boundary between two mesoperthite grains and the Rt1. The nature of this grain was examined with EBSD, and it was not a match for an aluminosilicate (e.g., kyanite or mullite) and was determined to be most likely a hydrated aluminosilicate mineral.

Nine analyses of Rt1 yielded a discordant array of ages with poorly defined upper and lower intercept ages of c. 1820 and 990 Ma, respectively (Figure 8a); one analysis was excluded due to excessively high common Pb. The nine analyses have Zr concentrations ranging from 551 to 663 ppm yielding temperatures of between 691°C and 703°C (Figure 8b).

4.2.2 | Rutile Grain 2 (Rt2)

Rt2 was also located within a leucosome and is enclosed entirely within mesoperthite (Figure 7b). BSE images highlight the grain contains high response needles that appear to show a preferred orientation within the rutile host. Elemental mapping of Rt2 shows that the high response BSE needles are depleted in Ti and enriched in Zr and Si relative to the rutile host (Figure 7b,f,j,n) and are interpreted to be zircon exsolved from the rutile host during cooling.

Ten analyses from Rt2 yield a cluster of eight concordant ages at c. 1800 Ma and when combined with the remaining two discordant ages yield a poorly defined lower intercept age at c. 1100 Ma (Figure 8a). The 10 analyses have Zr concentrations ranging from 7,840 to 9,690 ppm yielding temperatures of between 991°C and 1,026°C (Figure 8b).
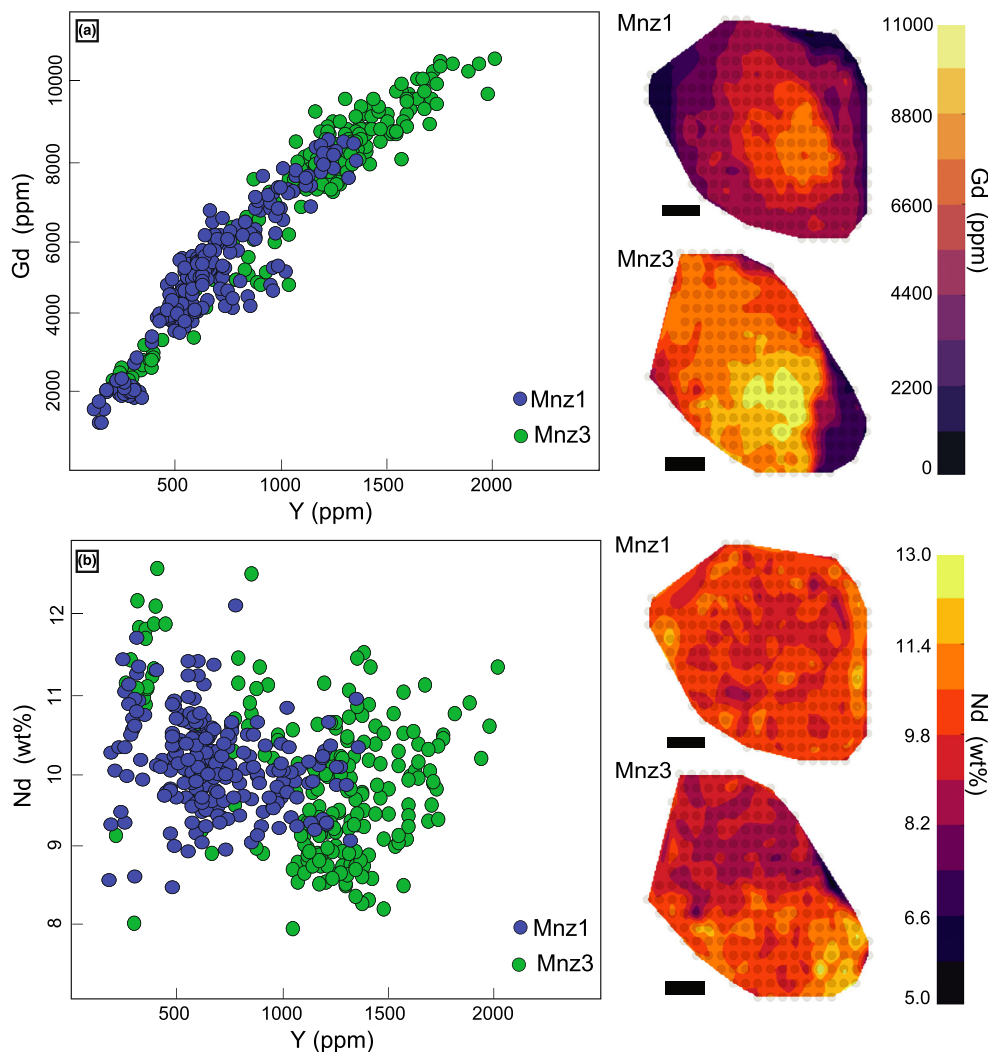
FIGURE 6 Gadolinium and neodymium elemental plots and maps for leucosome-hosted monazite grains illustrating the areas of relative enrichment and depletion and the degree of covariance with yttrium.

4.2.3 | Rutile Grain 3 (Rt3)

Rt3 sits within the aluminous residuum of the sample (Figure 2a) and is in contact with garnet, quartz and sillimanite. An acicular zircon grain is in contact with the Rt3 along the upper left of the grain (Figure 7c). The BSE response of the grain is uniform throughout the grain (Figure 7c) as are the Ti, Zr and Si elemental maps (Figures 7g,k,o).

Nine analyses from Rt3 return two near concordant ages at c. 1650 Ma and seven discordant ages that yield a lower intercept age of 735 ± 124 Ma (Figure 8a). The nine analyses have Zr concentrations ranging between 491 and 846 ppm yielding temperatures between 681°C and 730°C (Figure 8b).

4.2.4 | Rutile Grain 4 (Rt4)

Rt4 is situated within the leucosome in contact with quartz, mesoperthite and a garnet grain (Figure 7d). A

BSE image shows the grain contains high response needles that appear to show a preferred orientation within the rutile host. Elemental mapping of Rt4 shows that the high response BSE needles are depleted in Ti and enriched in Zr and Si relative to the rutile host (Figure 7b,h,l,p) and are interpreted to be zircon exsolved from the rutile host during cooling.

Fourteen analyses from Rt4 yield a cluster of 10 concordant ages at c. 1800 Ma and when combined with the remaining four discordant ages yield a poorly defined lower intercept age at c. 1100 Ma (Figure 8a). The 14 analyses have Zr concentrations ranging from 8,640 to 13,770 ppm yielding temperatures of between 1,006°C and 1,080°C (Figure 8b).

4.3 | Zircon

The 31 analyses acquired from 20 zircon grains from Sample 11178/4 can be divided in to two populations based on their Yb/Gd slopes on the REE plots in
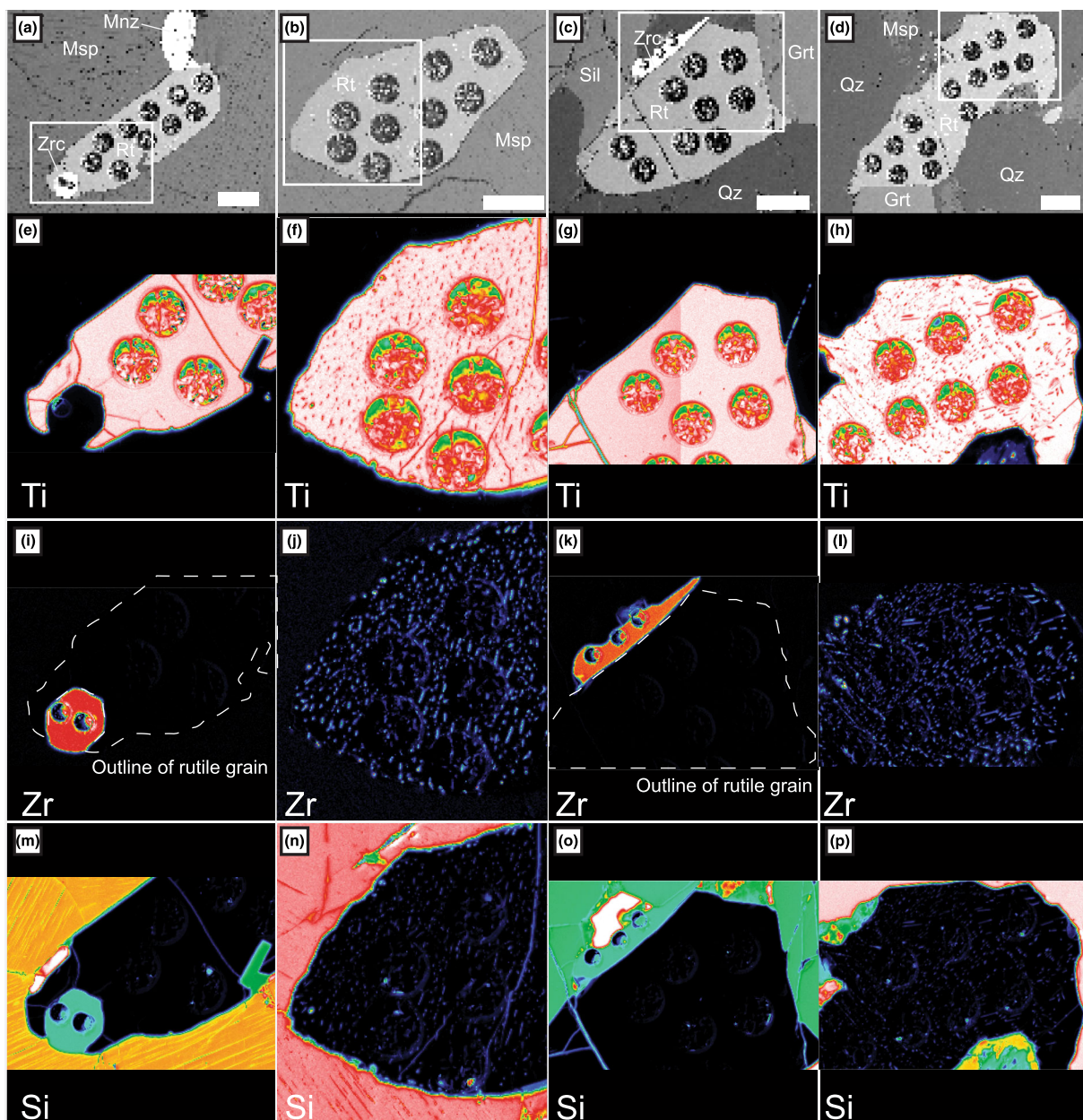
FIGURE 7 (a–d) BSE images of rutile grains analysed in this study (a) Rt1, (b) Rt2, (c) Rt3 and (d) Rt4. White boxes in each image demarcate the areas where EPMA mapping was undertaken. Scale bar is 100 μm (e–h) EPMA map of Ti distribution in analysed rutile grains. (i–l) EPMA maps of Zr distribution in rutile grains. (m–p) EPMA maps od Si distribution in rutile grains.

Figure 8d. Twenty-three analyses have Yb/Gd < 2 and are interpreted to be metamorphic in origin. These yield a weighted mean ^{207}Pb–^{206}Pb age of 2442 ± 4 Ma (MSWD 0.33, $n = 23$; Figure 8c). These grains have pronounced Eu* anomalies (0.15–0.80 but generally <0.6) and have Ti concentrations of between 15 and 48 ppm yielding a range of temperatures between 785°C and 945°C (Figure 8d). The remaining eight analyses have Yb/Gd ratios of >4, Ti concentrations ranging from 28 to 56 ppm and a range of ^{207}Pb–^{206}Pb ages from 2439 to 2791 Ma with one of those analyses being discordant.

4.4 | Garnet

All six garnet grains analysed have Yb/Gd ratios <1 displaying flat chondrite normalized rare earth patters when plotted on a Matsuda diagram (Figure 8f) with Grt2 displaying a slightly concave up pattern rather than flat. All grains display a well-developed negative Europium anomaly. Individual garnet grains varied in absolute Y concentration with all grains apart from Grt2 containing between 100 and 250 ppm (Figure 8e). The Y concentration measured in Grt2 ranged from 62 to 101 ppm (Figure 8e).
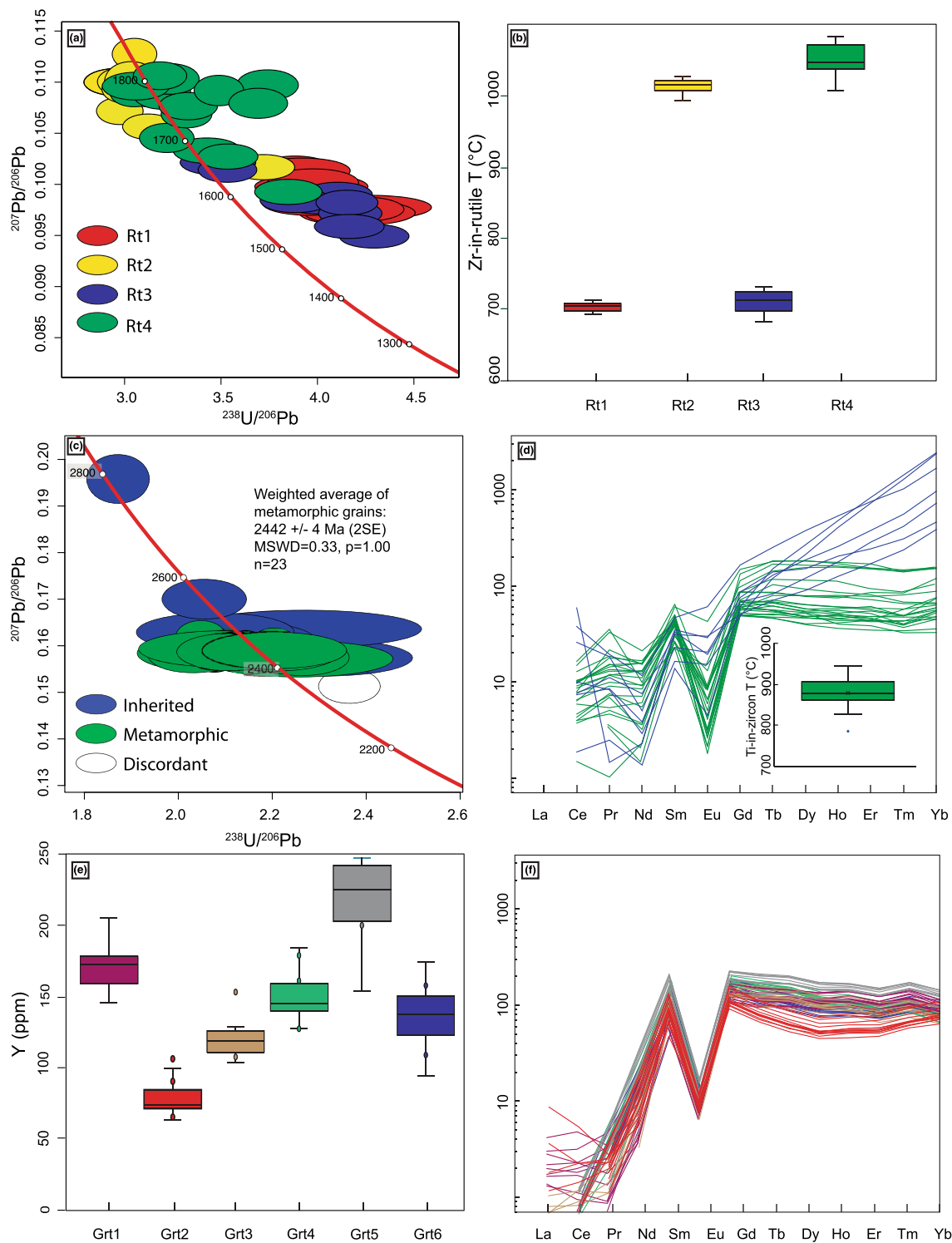
FIGURE 8 (a) Tera-Wasserberg concordia diagram for rutile geochronology, colour coded by individual grain. (b) Zirconium-in-rutile thermometry retrieved from individual rutile grains. (c) Tera-Wasserberg concordia diagram for zircon, analyses sorted by textural position of analysis and degree of discordance. (d) Chondrite-normalized REE diagram for zircon grain, colours match ellipses from corresponding concordia diagram. (e) Yttrium contents of individual garnet grains analysed. (f) Chondrite-normalized REE diagram for garnet grain; colours match ellipses from yttrium distribution plot.

WILEY 969

5 | DISCUSSION

5.1 | Modification of monazite

The monazite grains analysed in this study yield a complex array of ages that can be correlated with their microtextural positions within the rock and potentially interpreted in terms of the microstructural setting of the individual grain. The modification of the monazite grains can be separated in to two processes. The first is a high-temperature diffusion-driven process that proceeded after the crystallization of the monazite grains but during the same protracted ultrahigh- to high-T metamorphic event. The second is localized intragrain recrystallisation that occurred in the presence of a fluid phase c. 700 Myr after the main thermal event. The evidence for these processes and the implications for monazite petrochronology more generally will be discussed in the following sections and is illustrated schematically in Figure 9.

5.1.1 | Isotopic disturbance in high-temperature monazite

The most obvious feature of the geochronological investigations in this study is the preservation of the oldest concordant ages in monazite grains (Mnz2 and Mnz4) that are effectively armoured by a host mineral (Figure 3a). The age preserved in the two monazite grains is equivalent within error at c. 2485 Ma, older than the U–Pb zircon age of 2442 ± 4 Ma that has been obtained from leucosome-hosted zircon. The textural position and age indicate that the armoured monazite grew during prograde to peak metamorphism; the trigger for the growth of monazite is potentially driven by the incongruent dissolution of apatite in to melt resulting in phosphorous saturation (Wolf & London, 1994). This mechanism of monazite growth has to be previously inferred for prograde monazite growth in high-grade terranes in India (Johnson et al., 2015) and the Sierra de Quilmes of Argentina (Weinberg et al., 2020). Yakymchuk (2017) evaluated this mechanism through thermodynamic modelling and concluded that the growth of monazite from dissolving apatite is likely ineffective at higher temperatures where diffusion and melt homogenization would occur and any prograde monazite would be dissolved. Yakymchuk (2017) suggest that the upper limit for this process is ∼850°C; this requires the garnet in this study to have grown on the prograde path rather from melt crystallization in order to shield the early monazite from redissolution and the monazite age to constrain progade metamorphism rather than the peak. The concordant spot age distributions within armoured grains can,

for the most part, be interpreted in terms of a control by flux limited diffusion (e.g., Kohn et al., 2016; Smye et al., 2018). In this case, both Mnz2 and Mnz4 are entirely enclosed within a single mineral, and, at least in 2D, the inter-grain boundaries are not connected with the grain boundary network within the rock. This microstructural setting means that there is no mechanism to facilitate grain boundary mass transport of Pb away from the armoured monazite grains. In addition, the armouring minerals are unlikely to act as sinks for Pb, which therefore is unable to escape the monazite.

By contrast, Mnz1 and Mnz3 have a range of concordant ages that stretch from 2440 to 2200 Ma. The upper age limit for the unarmoured grains is similar to that of the younger overgrowth age on Mnz4 (c. 2434 Ma) and the zircon age from within the sample ($2,442 \pm 4$ Ma). The younger ages and textural position along grain boundaries within the minerals that comprise the leucosome suggest that these monazite grains grew from crystallizing melt as the rock cooled towards an elevated solidus. This style of growth and the age discrepancy between the zircon and monazite are consistent with theoretical predictions of studies of accessory mineral growth from crystallizing melt (Kelsey et al., 2008; Yakymchuk et al., 2017; Yakymchuk & Brown, 2014). In addition, the age of monazite recorded in this sample is within error of the monazite age reported by Black et al. (1984) from Zircon Point in the Field Islands. A second feature of the unarmoured monazite grains is that they display a more complex pattern of ages that indicate that the growth ages have been disturbed by post-crystallization processes. When the spot ages of these grains are plotted in map form (Figure 4b), both Mnz1 and Mnz3 show age zonation that has younger interiors and older exteriors. The analyses are within uncertainty of concordia down to c. 2200 Ma but increase in discordance with decreasing age. A free regression through the analyses from Mnz1 and Mnz3 yields an upper intercept age of c. 2450 Ma and a lower intercept ages of 1732 ± 54 Ma and 1793 ± 45 Ma, respectively. The precision of the estimates on the lower intercept is complicated by the large spread of concordant ages between 2450 and 2200 Ma; however, it is clear that the grains underwent a Pb-loss event in the late-Palaeoproterozoic. Previous geochronological investigations of the Napier Complex are mostly focused on zircon, and all report metamorphic ages in the 2400–2500 Ma range with a number of studies capturing imprecise lower intercepts at c. 1000 and 500 Ma. However, one study by Carson et al. (2002) identified a concordant zircon at c. 1800 Ma through the application of ion-probe depth profiling and suggest that it is the result of a zircon growth or complete isotopic resetting event of this age. The Palaeoproterozoic
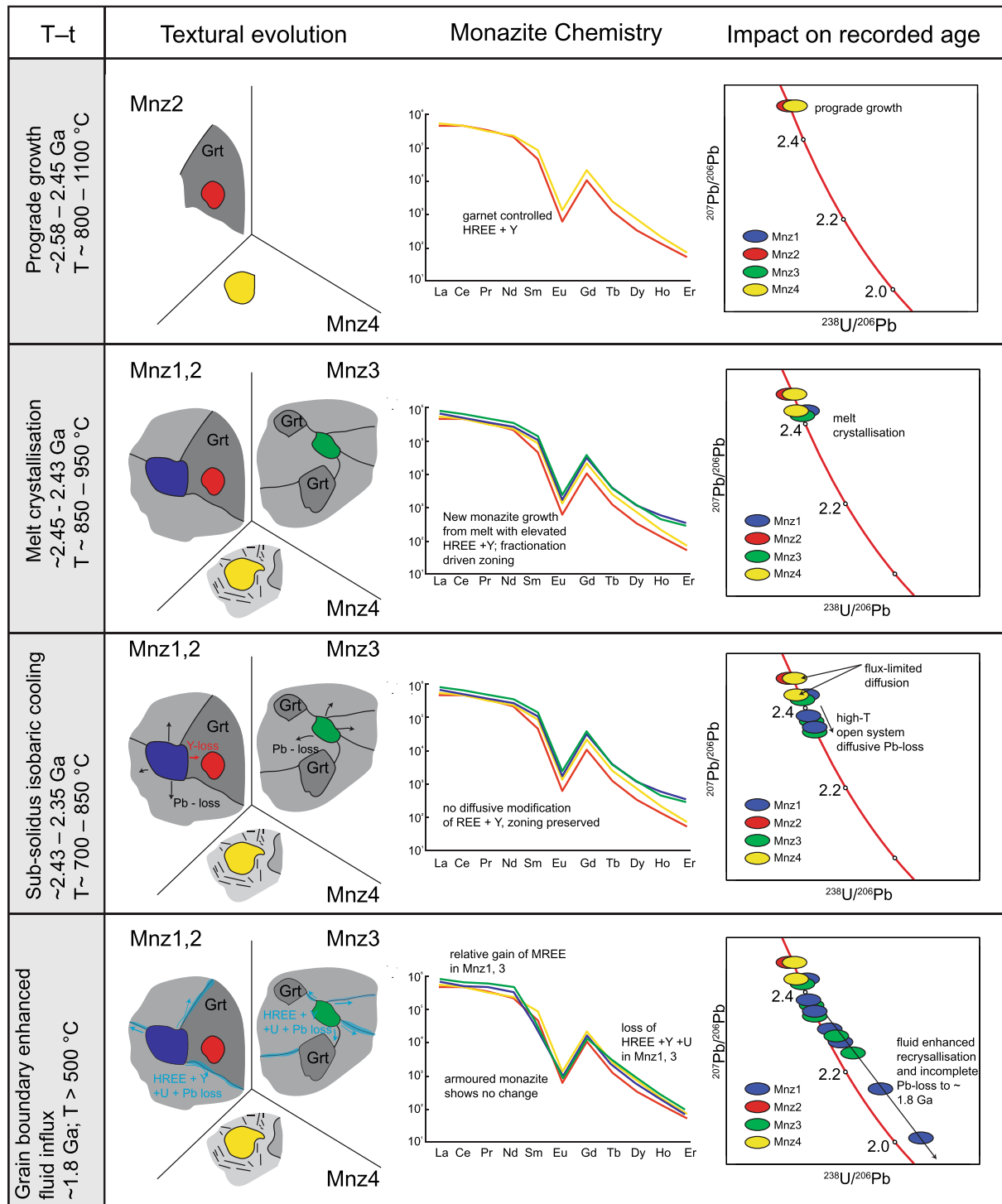
FIGURE 9 Schematic illustration summarizing the growth, evolution and role of microstructural setting of monazite grains in terms of the resulting REE patterns and geochronological data obtained from individual grains examined in this study.

age is consistent with the upper intercept age of rutile grains from the sample and the formation of the exsolved zircon within the rutile. The implications this observation has for the thermal evolution of the Dallwitz Nunatak region, and the Napier Complex more broadly will be discussed in the final section.

5.1.2 | Geochemical disturbance in high-temperature monazite

In addition to the differing isotopic behaviour of monazite grains, each grain has a different preserved geochemical pattern. These differing compositional patterns can

again be related to their microstructural location, whether it be armoured in a grain, sitting on grain boundaries or the proximity to different minerals. The armoured monazite grains Mnz2 and Mnz4 preserve relatively homogenous HREE and Y compositions. Grain Mnz2, which is armoured in a single garnet grain, has the lowest concentration of Y. The homogeneity of the Y concentration in Mnz2 could be either a primary growth feature or the result of diffusion-controlled equilibration within the armoured monazite grain. Grain Mnz4, which exhibits homogeneous chemistry over most of the grain, has an elevated Y content in the c. 2480 age domain and lower Y in the younger age protuberance. This leads us to the preferred interpretation that the observed lack of Y zonation in armoured monazite reflects diffusional equilibration of monazite within the armouring mineral, whereby garnet acts as a sink for Y resulting in lower Y contents in Mnz2 compared to the quartz-armoured Mnz4.

The monazite grains sitting in the matrix preserve zoning in Y with the main difference being that the Mnz1 has a lower absolute Y and HREE concentrations than Mnz3. This lower absolute concentration most likely results from Mnz3 being in contact with garnet, whereas Mnz1 sits at the junction of three perthite grains. The preservation of Y and HREE zoning in the matrix monazite grains when compared armoured grains, Mnz2 and Mnz4, is consistent with the younger ages of the matrix monazite and the interpretation that they grew during the cooling of the rock through the solidus. The lowest concentrations of Y and HREE are observed where the monazite grains are in proximal to the junction of multiple grain boundaries.

When combined, these observations are consistent with the suggestion that the mineral in contact with monazite seems to exerts a control over both the intra-grain distribution of age and chemistry as proposed by Grew et al. (2008) in their study on the nearby rocks of Mount Pardoe. Grew et al. (2008) proposed that Pb diffusion, and related discordance in the U–Pb system, will be enhanced if a Pb sink (e.g., mesoperthite) is proximal to the grain. In contrast, the geochemical characteristics are most susceptible to modification by either being in direct contact with a mineral with higher affinity for an element (e.g., Y and HREE in garnet) or where the mineral is sitting at the junction of a grain boundary. The grain boundary related modification in the case of the monazite at Dallwitz Nunatak is interpreted to represent fluid enhanced recrystallization during a subsequent thermal event rather than a purely solid-state diffusion-controlled process. Supporting evidence for this fluid related interpretation will be discussed in the final section of the discussion.

5.2 | Implications for monazite petrochronology in high-grade rocks

The isotopic and geochemical patterns recorded in the monazite grains from Dallwitz Nunatak have implications for how previous studies have coupled these datasets in order to develop petrochronological frameworks for the evolution of high-grade rocks. The results presented here demonstrate that individual monazite grains within a single sample can record varying degrees of decoupling between the age and chemical compositions. Decoupling of U–Pb and Th, U and Ti at high temperatures has been documented in zircon from a sample set from the Ivrea Zone although the relationship between age and REE decoupling was less clear (Kunz et al., 2018). By contrast, the results from this study demonstrate that age and chemistry can be decoupled within a single sample in a high temperature rock. Obviously, this has implications for how to approach interpretation of the isotopic and geochemical systems to constrain the age of thermal events in high-grade metamorphic rocks particularly with reference to the use of garnet–monazite REE partitioning ($D_{Mnz/Grt}$).

5.2.1 | Towards robust $D_{Mnz/Grt}$ values for suprasolidus metamorphic rocks

A number of studies have attempted to devise a systematic framework for how monazite partitions HREE with garnet during metamorphism (Buick et al., 2006; Hermann & Rubatto, 2003; Jiao et al., 2021; Mottram et al., 2014; Rubatto et al., 2006; Warren et al., 2019). Figure 10 illustrates empirically derived constraints on equilibrium partitioning between monazite and garnet pairs from a number of studies at both subsolidus and suprasolidus conditions. In addition, the figure includes data from the study by Hacker et al. (2019) where equilibrium partitioning is derived via the temperature dependence of partitioning based on Y and HREE relationships. As can be seen in Figure 10, there is considerable variation in the studies but some consistency in sub-solidus amphibolite facies partitioning both between studies and the predictions based on the Hacker et al. (2019) study.

Figure 10 also includes plotted data illustrating the relationship between $D_{Mnz/Grt}$ values for a set of UHT granulites, alongside the partitioning values for the Mnz2–Grt2 pair as measured in this study. Notably, the observed UHT $D_{Mnz/Grt}$ values significantly deviate from the anticipated relationship proposed by Hacker et al. (2019). Contrary to the predicted progressive increase in $D_{Mnz/Grt}$ values with rising temperature suggested by Hacker et al. (2019), the values obtained from UHT rocks are notably lower compared to those observed
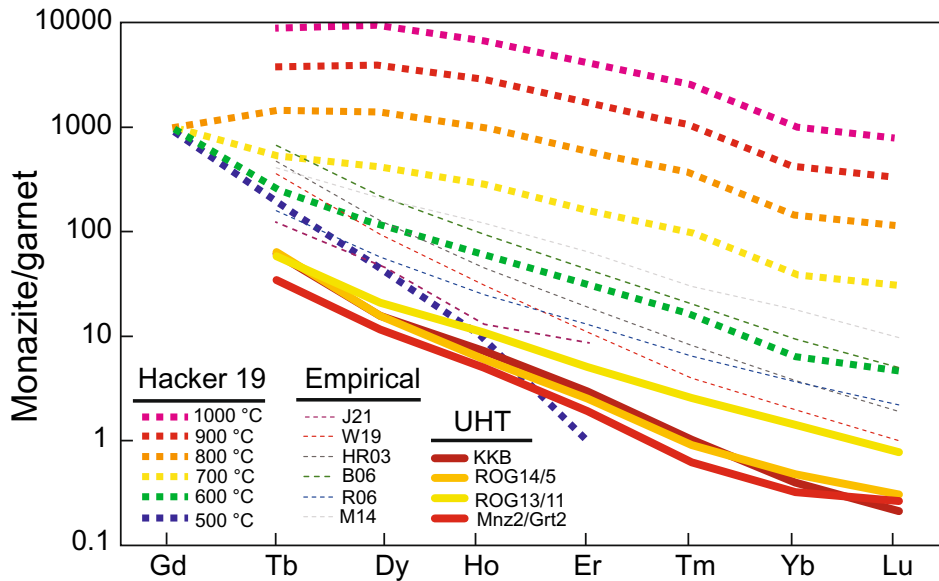
FIGURE 10 Monazite–garnet HREE partitioning ($D_{Mnz/Grt}$) reported in previous studies: W19, Warren et al. (2019); B06, Buick et al. (2006); HR03, Hermann and Rubatto (2003); M14, Mottram et al. (2014); R06, Rubatto et al. (2006); J21, Jiao et al. (2021). Derived from the relationships presented in Hacker et al. (2019). Published data from UHT rocks: KKB, Blereau et al. (2016); Rog14/5 and ROG13/11, Blereau et al. (2017); and the Grt2/Mnz2 data presented in this paper. Y axis is a dimensionless ratio. Data for plot are tabulated in Table S5.

or predicted in prior studies. The closest match to the $D_{Mnz/Grt}$ values measured in this study is found in sample ROG14/5 from the investigation by Blereau et al. (2017), which focused on a garnet-bearing metapelite located at the contact with the Rogaland Anorthosite. This sample, akin to the Napier Complex, likely represents crustal rocks approaching their maximum achievable temperatures. The consistency between the data derived from garnet-hosted monazite in our study and other datasets from UHT terranes suggests that our partitioning relationships define the $D_{Mnz/Grt}$ values at temperatures around 1,000°C. Interestingly, $D_{Mnz/Grt}$ values from studies involving rocks subjected to partial melting or interpreted as having undergone granulite facies metamorphism exhibit similar relationships. For instance, Jiao et al.'s (2021) study, which infers temperatures just overlapping the onset of UHT conditions (830–980°C), shows intermediate values compared to those from upper amphibolite to granulite studies conducted by Buick et al. (2006), Hermann and Rubatto (2003) and Rubatto et al. (2006), as well as data from higher temperature UHT rocks, indicating that there may be a systematic relationship with increasing temperatures in suprasolidus rocks. The discrepancy between this observed relationship and the one predicted by Hacker et al. (2019) for sub-solidus rocks suggests an avenue worthy of exploration, possibly through carefully controlled experimental work.

petrographic context of individual grains. These relationships cannot be evaluated if the grains are separated during geochronological investigations. An important factor to consider here is the influence of neighbouring minerals on the potential loss of Pb. In this study, grains in contact with mesoperthite demonstrate a pattern of Pb-loss that is not observed in grains not adjacent to mesoperthite. This relationship was previously documented at Zircon Point in the Casey Bay region by Grew et al. (2008). They noted Pb-enrichment in surrounding feldspars and linked it to discordant monazite analyses from SHRIMP U–Pb data reported by Black et al. (1984), as well as the wide range of monazite spot ages from various locations analysed by EPMA in the study conducted by Asami et al. (2002).

Interestingly, EPMA age data from Asami et al.'s (2002) sample MA88022102 from Mount Riiser Larsen, which is closest to our Sample 11178/4, exhibits spot age populations that are similar to the discordant ages observed in our study. However, without isotopic data providing a measure of concordance, the processes leading to the younger ages observed in the EPMA study would remain speculative. This underscores the challenges associated with EPMA monazite geochronology in high-UHT metamorphic rocks or in cases where post-monazite growth fluid-related processes have occurred, indicating that caution should be exercised when interpreting results from studies presenting this type of data.

5.2.2 | Discordance generation and implication for geochronological techniques

Monazite grains display various age–trace element relationships that systematically vary based on the

5.3 | Petrochronological constraints on the evolution of Dallwitz Nunatak

The geochronological data from zircon, monazite and rutile in the metapelite from Dallwitz Nunatak allow for

a refined history of the rocks and potentially the region to be constructed. Early monazite grew contemporaneously with garnet at c. 2.48 Ga providing a maximum age constraint on UHT conditions in the area. This age constraint for UHT is younger than ages from previous studies of the Casey Bay region where leucosome-hosted zircon is inferred to constrain the attainment of high-grade conditions at c. 2.56 Ga (Harley, 2016; Harley et al., 2001). However, there is very little evidence of this older event in the bulk of ages from across the Amundsen Bay area, where the current sample is located. This leads to our preferred interpretation of UHT conditions in this area being achieved at c. 2.48 Ga and this being the best constraint on the onset of UHT conditions in this area of the Napier Complex. The Zr-in-rutile data from grains where zircon have exsolved within the grain constrain the peak temperatures in this sample to be >1,000°C during the UHT event.

Zircon grains preserve perhaps the simplest age, trace element and thermometric relationships in that the grains with the low Yb/Gd ratios, interpreted to be grown in equilibrium with the garnet in the rock, return a weighted mean ^{207}Pb–^{206}Pb age of 2442 ± 4 Ma and Ti-in-zircon temperatures of between 785°C and 945°C. This age, temperature and trace element information fits with the previous petrochronological datasets for this area presented in Clark et al. (2018). In that study, the age and Ti-in-zircon temperatures were interpreted to reflect zircon growth during leucosome crystallization during post-UHT cooling with the high temperatures reflecting the elevated solidus within the melt-depleted rocks. This interpretation is consistent with the observation that the bulk of zircon grains occur within the leucosome or at the interface between leucosome and metapelitic residuum in Sample 11178/4 (Figure 2e).

Whilst more complicated, the discordant arrays of monazite data observed in the leucosome hosted grains can be potentially interpreted in two ways. The first is that monazite was open to diffusive Pb-loss during a protracted slow cooling from the peak UHT to c. 2 Ga and a second interpretation is that Pb-loss was facilitated by a thermal and fluid infiltration event at c. 1.8 Ga. The geochemical patterns whereby the monazite age and chemistry are modified to greatest degree where grain boundaries are present, and the coincidence of the lower intercept of monazite ages with the upper intercept returned from the rutile in the sample lead us to favour the second option. This discrete thermal event at c. 1.8 Ga has not been previously documented in the rocks of the Amundsen Bay region although a few studies have identified similar ages that have been interpreted as discordance or new growth at this time. A discrete thermal episode is also supported by Sm–Nd and Lu–Hf whole rock isochrons, suggesting that the rocks had cooled below the closure temperatures for these systems by c. 2.38 Ga. (Choi et al., 2006; Suzuki et al., 2006) and therefore require a reheating event to modify the isotopic systematics of rutile and monazite to the degree observed in the sample from Dallwitz Nunatak.

The rutile grains examined in this study display a complex array of internal textures, ages and Zr-in-rutile temperatures. Two types of petrographically distinct types of rutile can be observed. Type 1 rutile containing crystallographically controlled exsolution of zircon (grains Rt2 and Rt4) and Type 2 exsolution-free rutile in contact with zircon (grains Rt1 and Rt3). Type 1 rutile preserves concordant to mildly discordant ages ranging between c. 1700 and 1800 Ma and record temperatures of ~1,000°C. By contrast, Type 2 rutile grains form a discordant array with an upper intercept at c. 1700 Ma and a poorly defined lower intercept at c. 1000 Ma. These grains also yield a considerably lower Zr-in-rutile temperature of ~700°C. Whilst it is clear from their microtextural settings that all rutile grains formed during the UHT stage of metamorphism at c. 2450 Ma, the age data indicate that they underwent complete resetting at c. 1800 Ma. Moreover, the inclusion of a hydrous aluminosilicate mineral in grain Rt1 at a grain boundary junction suggests that the rutile grains interacted with a fluid subsequent to their growth, consistent with the presence of occasional myrmekitic intergrowths formed at the expense of perthite. An interpretation of how the two types of grains now record such different Zr-in-rutile temperatures is that during fluid infiltration at c. 1800 Ma, the rutile grains in contact with zircon were able to equilibrate their Zr composition with the adjacent zircon grain at the temperature of the fluid event at ~700°C. This is achieved by Zr exsolving from the rutile grain and reprecipitating as films on the proximal zircon. The temperature was high enough during the c.1800 Ma event to reset the U–Pb system within the grains. By contrast, rutile grains with no proximal zircon grain to act as a reservoir for the excess Zr in the grain exsolved the observed zircon rods. As fluid was present during this event, Si was able to be sourced from the Si saturated leucosome, and zircon could be stabilized rather than baddeleyite. The exsolution of zircon fixed the Zr composition of the grains and when sampled during analysis yielded the pre-exsolution UHT temperature of the original rutile grain. The differing degrees of discordance observed in the Types 1 and 2 rutile grains can be attributed to partial resetting during the widely recognized Mesoproterozoic thermal event that has been previously reported to have affected the Napier Complex and is observed to affect the monazite grains. In effect, the dates returned from Type 1 rutile are moderated by the exsolved zircon, which, due

to its higher closure temperature, remained closed to Pb-loss, whereas Type 2 rutile grains, which do not contain exsolved 1800 Ma zircon, were open to Pb-loss to a greater degree.

6 | CONCLUSIONS

1. The data from this study identify two primary modification processes of monazite in high-grade metamorphic rocks: diffusion-driven events post-crystallization and localized intragrain recrystallization in the presence of fluid after the UHT event.
2. Armoured monazite grains, protected by host minerals, preserved the oldest ages indicating growth during peak metamorphism, likely due to phosphorous saturation from the incongruent dissolution of apatite.
3. Unarmoured monazite grains showed a broader range of ages, suggesting growth from crystallizing melt during cooling and disturbance by post-crystallization events, including a significant late-Palaeoproterozoic Pb-loss event. This event was also observed in the resetting of rutile grains.
4. Geochronology from monazite reflects that both the preservation of older ages in armoured grains and the complex age patterns in unarmoured grains are indicative of initial growth conditions and subsequent modification events. By contrast, the geochronological and trace element systematics of zircon seem to be unaffected by post crystallization thermal and fluid events.
5. The armoured monazite grain allows for a robust estimate of the heavy rare earth element (HREE) partitioning between monazite and garnet in ultrahigh-temperature conditions to be developed. The resulting values are not consistent with previous empirically derived relationships showing a decrease, rather than an increase, in $D_{Mnz/Grt}$ values with temperature.

- This study highlights the importance of considering microstructural context and mineral interactions in interpreting monazite geochemistry and age data, especially in high-grade metamorphic rocks, to reconstruct metamorphic histories accurately.
- Through a combination of the information derived from the analysis of multiple accessory minerals, a refined history of the Amundsen Bay region in the Napier Complex can be constructed. The rocks in this region show no evidence of the early (c. 2.56 Ga) UHT event documented in the Casey Bay area, a c. 1.8 Ga thermal event that resets the U–Pb system, and to a limited degree, the trace elements in rutile is also identified.

ORCID

Chris Clark https://orcid.org/0000-0001-9982-7849
Simon L. Harley https://orcid.org/0000-0002-1903-939X

REFERENCES

Aleinikoff, J. N., Schenck, W. S., Plank, M. O., Srogi, L., Fanning, C. M., Kamo, S. L., & Bosbyshell, H. (2006). Deciphering igneous and metamorphic events in high-grade rocks of the Wilmington complex, Delaware: Morphology, cathodoluminescence and backscattered electron zoning, and SHRIMP U-Pb geochronology of zircon and monazite. *Bulletin of the Geological Society of America*, *118*(1–2), 39–64. https://doi.org/10.1130/B25659.1

Anders, E., & Grevesse, N. (1989). Abundances of the elements: Meteoritic and solar. *Geochimica et Cosmochimica Acta*, *53*(1), 197–214. https://doi.org/10.1016/0016-7037(89)90286-X

Asami, M., Suzuki, K., & Grew, E. S. (2002). Chemical Th-U-total Pb dating by electron microprobe analysis of monazite, xenotime and zircon from the Archean Napier complex, East Antarctica: Evidence for ultra-high-temperature metamorphism at 2400 Ma. *Precambrian Research*, *114*(3–4), 249–275. https://doi.org/10.1016/S0301-9268(01)00228-5

Baldwin, J. A., Brown, M., & Schmitz, M. D. (2007). First application of titanium-in-zircon thermometry to ultrahigh-temperature metamorphism. *Geology*, *35*(4), 295–298. https://doi.org/10.1130/G23285A.1

Black, L. P., Fitzgerald, J. D., & Harley, S. L. (1984). Pb isotopic composition, colour, and microstructure of monazzites from a polymetamorphic rock in Antarctica. *Contributions to Mineralogy and Petrology*, *85*, 141–148. https://doi.org/10.1007/BF00371704

—**WILEY**—

Blereau, E., Clark, C., Taylor, R. J. M., Johnson, T. E., Fitzsimons, I. C. W., & Santosh, M. (2016). Constraints on the timing and conditions of high-grade metamorphism, charnockite formation and fluid-rock interaction in the Trivandrum block, southern India. *Journal of Metamorphic Geology*, *34*(6), 527–549. https://doi.org/10.1111/jmg.12192

Blereau, E., Johnson, T. E., Clark, C., Taylor, R. J. M., Kinny, P. D., & Hand, M. (2017). Reappraising the P-T evolution of the Rogaland-Vest Agder sector, southwestern Norway. *Geoscience Frontiers*, *8*(1), 1–14. https://doi.org/10.1016/j.gsf.2016.07.003

Buick, I. S., Hermann, J., Williams, I. S., Gibson, R. L., & Rubatto, D. (2006). A SHRIMP U–Pb and LA-ICP-MS trace element study of the petrogenesis of garnet–cordierite–orthoamphibole gneisses from the central zone of the Limpopo Belt, South Africa. *Lithos*, *88*(1), 150–172.

Carson, C. J., Ague, J. J., Grove, M., Coath, C. D., & Harrison, T. M. (2002). U-Pb isotopic behaviour of zircon during upper-amphibolite facies fluid infiltration in the Napier Complex, East Antarctica. *Earth and Planetary Science Letters*, *199*(3–4), 287–310. https://doi.org/10.1016/S0012-821X(02)00565-4

Cherniak, D. J., & Pyle, J. M. (2008). Th diffusion in monazite. *Chemical Geology*, *256*(1–2), 52–61. https://doi.org/10.1016/j.chemgeo.2008.07.024

Cherniak, D. J., Watson, E. B., Grove, M., & Harrison, T. M. (2004). Pb diffusion in monazite: A combined RBS/SIMS study. *Geochimica et Cosmochimica Acta*, *68*(4), 829–840. https://doi.org/10.1016/j.gca.2003.07.012

Choi, S. H., Mukasa, S. B., Andronikov, A. V., Osanai, Y., Harley, S. L., & Kelly, N. M. (2006). Lu–Hf systematics of the ultra-high temperature Napier Metamorphic Complex in Antarctica: Evidence for the early Archean differentiation of Earth's mantle. *Earth and Planetary Science Letters*, *246*(3-4), 305–316.

Clark, C., Taylor, R. J. M., Johnson, T. E., Harley, S. L., Fitzsimons, I. C. W., & Oliver, L. (2019). Testing the fidelity of thermometers at ultrahigh temperatures. *Journal of Metamorphic Geology*, *37*(7), 917–934. https://doi.org/10.1111/jmg.12486

Clark, C., Taylor, R. J. M., Kylander-Clark, A. R. C., & Hacker, B. (2018). Prolonged (>100 Ma) ultrahigh temperature metamorphism in the Napier Complex, East Antarctica: A petrochronological investigation of Earth's hottest crust. *Journal of Metamorphic Geology*, *36*(9), 1117–1139. https://doi.org/10.1111/jmg.12430

Dallwitz, W. B. (1968). Co-existing Sapphirine and quartz in granulite from Enderby Land, Antarctica. *Nature*, *219*, 476–477. https://doi.org/10.1038/219476a0

Donovan, J. J., & Tingle, T. N. (1996). An improved mean atomic number background correction for quantitative microanalysis. *Microscopy and Microanalysis*, *2*(1), 1–7.

Donovan, J. J., Snyder, D. A., & Rivers, M. L. (1993). An improved interference correction for trace element analysis. *Microbeam Analysis*, *2*, 23–28.

Dumond, G., Goncalves, P., Williams, M. L., & Jercinovic, M. J. (2015). Monazite as a monitor of melting, garnet growth and feldspar recrystallization in continental lower crust. *Journal of Metamorphic Geology*, *33*(7), 735–762. https://doi.org/10.1111/jmg.12150

Ellis, D. J. (1980). Osumilite-sapphirine-quartz granulites from Enderby Land, Antarctica: P-T conditions of metamorphism, implications for garnet-cordierite equilibria and the evolution of the deep crust. *Contributions to Mineralogy and Petrology*, *74*(2), 201–210. https://doi.org/10.1007/BF01132005

Erickson, T. M., Pearce, M. A., Taylor, R. J. M., Timms, N. E., Clark, C., Reddy, S. M., & Buick, I. S. (2015). Deformed monazite yields high-temperature tectonic ages. *Geology*, *43*(5), 383–386. https://doi.org/10.1130/G36533.1

Ferry, J. M., & Watson, E. B. (2007). New thermodynamic models and revised calibrations for the Ti-in-zircon and Zr-in-rutile thermometers. *Contributions to Mineralogy and Petrology*, *154*(4), 429–437. https://doi.org/10.1007/s00410-007-0201-0

Foster, G., Gibson, H. D., Parrish, R., Horstwood, M., Fraser, J., & Tindle, A. (2002). Textural, chemical and isotopic insights into the nature and behaviour of metamorphic monazite. *Chemical Geology*, *191*, 183–207. https://doi.org/10.1016/S0009-2541(02)00156-0

Fougerouse, D., Reddy, S. M., Saxey, D. W., Erickson, T. M., Kirkland, C. L., Rickard, W. D. A., Seydoux-Guillaume, A. M., Clark, C., & Buick, I. S. (2018). Nanoscale distribution of Pb in monazite revealed by atom probe microscopy. *Chemical Geology*, *479*, 251–258. https://doi.org/10.1016/j.chemgeo.2018.01.020

Grand'Homme, A., Janots, E., Seydoux-Guillaume, A. M., Guillaume, D., Bosse, V., & Magnin, V. (2016). Partial resetting of the U-Th-Pb systems in experimentally altered monazite: Nanoscale evidence of incomplete replacement. *Geology*, *44*(6), 431–434. https://doi.org/10.1130/G37770.1

Grew, E. S., Yates, M. G., & Wilson, C. J. L. (2008). Aureoles of Pb (II)-enriched feldspar around monazite in paragneiss and anatectic pods of the Napier Complex, Enderby Land, East Antarctica: The roles of dissolution-reprecipitation and diffusion. *Contributions to Mineralogy and Petrology*, *155*(3), 363–378. https://doi.org/10.1007/s00410-007-0247-z

Hacker, B., Kylander-Clark, A., & Holder, R. (2019). REE partitioning between monazite and garnet: Implications for petrochronology. *Journal of Metamorphic Geology*, *37*(2), 227–237. https://doi.org/10.1111/jmg.12458

Harley, S. L. (2016). A matter of time: The importance of the duration of UHT metamorphism. *Journal of Mineralogical and Petrological Sciences*, *111*(2), 50–72. https://doi.org/10.2465/jmps.160128

Harley, S. L., & Black, L. P. (1997). A revised Archaean chronology for the Napier Complex, Enderby Land, from SHRIMP ion-microprobe studies. *Antarctic Science*, *9*(1), 74–91. https://doi.org/10.1017/S0954102097000102

Harley, S. L., & Hensen, B. J. (1990). Archaean and Proterozoic high-grade terranes of East Antarctica (40–80 E): A case study of diversity in granulite metamorphism. In J. R. Ashworth & M. Brown (Eds.), *High-temperature metamorphism and crustal anatexis* (pp. 320–370). Unwin Hyman. https://doi.org/10.1007/978-94-015-3929-6_12

Harley, S. L., Kinny, P. D., Snape, I., & Black, L. P. (2001). Zircon chemistry and the definition of events in Archaean granulite terrains, Fourth International Archaean Symposium, Extended Abstract Colume. *AGSO Geoscience Australia Record*, *2001*(37), 511–513.

Harley, S. L., & Motoyoshi, Y. (2000). Al zoning in orthopyroxene in a sapphirine quartzite: Evidence for >1120°C UHT metamorphism in the Napier Complex, Antarctica, and implications for the entropy of sapphirine. *Contributions to Mineralogy and Petrology*, 138(4), 293–307. https://doi.org/10.1007/s004100050564

Hermann, J., & Rubatto, D. (2003). Relating zircon and monazite domains to garnet growth zones: Age and duration of granulite facies metamorphism in the Val Malenco lower crust. *Journal of Metamorphic Geology*, 21(9), 833–852. https://doi.org/10.1046/j.1525-1314.2003.00484.x

Hokada, T., Motoyoshi, Y., Suzuki, S., Ishikawa, M., & Ishizuka, H. (2008). Geodynamic evolution of Mt. Riiser-Larsen, Napier Complex, East Antarctica, with reference to the UHT mineral associations and their reaction relations. *Geological Society, London, Special Publications*, 308(1), 253–282. https://doi.org/10.1144/SP308.13

Holder, R. M., Hacker, B. R., Horton, F., & Rakotondrazafy, A. F. M. (2018). Ultrahigh-temperature osumilite gneisses in southern Madagascar record combined heat advection and high rates of radiogenic heat production in a long-lived high-T orogen. *Journal of Metamorphic Geology*, 36(7), 855–880. https://doi.org/10.1111/jmg.12316

Holder, R. M., Hacker, B. R., Kylander-Clark, A. R. C., & Cottle, J. M. (2015). Monazite trace-element and isotopic signatures of (ultra)high-pressure metamorphism: Examples from the Western Gneiss Region, Norway. *Chemical Geology*, 409, 99–111. https://doi.org/10.1016/j.chemgeo.2015.04.021

Jackson, S. E., Pearson, N. J., Griffin, W. L., & Belousova, E. A. (2004). The application of laser ablation-inductively coupled plasma-mass spectrometry to in situ U-Pb zircon geochronology. *Chemical Geology*, 211(1–2), 47–69. https://doi.org/10.1016/j.chemgeo.2004.06.017

Jiao, S., Evans, N. J., Mitchell, R. N., Fitzsimons, I. C. W., & Guo, J. (2021). Heavy rare-earth element and Y partitioning between monazite and garnet in aluminous granulites. *Contributions to Mineralogy and Petrology*, 176(7), 50. https://doi.org/10.1007/s00410-021-01808-2

Jochum, K. P., Willbold, M., Raczek, I., Stoll, B., & Herwig, K. (2005). Chemical characterisation of the USGS reference glasses GSA-1G, GSC-1G, GSD-1G, GSE-1G, BCR-2G, BHVO-2G and BIR-1G using EPMA, ID-TIMS, ID-ICP-MS and LA-ICP-MS. *Geostandards and Geoanalytical Research*, 29(3), 285–302. https://doi.org/10.1111/j.1751-908X.2005.tb00901.x

Jochum, K. P., Wilson, S. A., Abouchami, W., Amini, M., Chmeleff, J., Eisenhauer, A., Hegner, E., Iaccheri, L. M., Kieffer, B., Krause, J., McDonough, W. F., Mertz-Kraus, R., Raczek, I., Rudnick, R. L., Scholz, D., Steinhoefel, G., Stoll, B., Stracke, A., Tonarini, S., ... Woodhead, J. D. (2011). GSD-1G and MPI-DING reference glasses for in situ and bulk isotopic determination. *Geostandards and Geoanalytical Research*, 35(2), 193–226. https://doi.org/10.1111/j.1751-908X.2010.00114.x

Johnson, T. E., Clark, C., Taylor, R. J. M., Santosh, M., & Collins, A. S. (2015). Prograde and retrograde growth of monazite in migmatites: An example from the Nagercoil block, southern India. *Geoscience Frontiers*, 6(3), 373–387. https://doi.org/10.1016/j.gsf.2014.12.003

Kelly, N. M., & Harley, S. L. (2005). An integrated microtextural and chemical approach to zircon geochronology: Refining the Archaean history of the Napier Complex, East Antarctica. *Contributions to Mineralogy and Petrology*, 149(1), 57–84. https://doi.org/10.1007/s00410-004-0635-6

Kelsey, D. E., Clark, C., & Hand, M. (2008). Thermobarometric modelling of zircon and monazite growth in melt-bearing systems: Examples using model metapelitic and metapsammitic granulites. *Journal of Metamorphic Geology*, 26(2), 199–212. https://doi.org/10.1111/j.1525-1314.2007.00757.x

Kohn, M. J., Penniston-Dorland, S. C., & Ferreira, J. C. S. (2016). Implications of near-rim compositional zoning in rutile for geothermometry, geospeedometry, and trace element equilibration. *Contributions to Mineralogy and Petrology*, 171(10), 78. https://doi.org/10.1007/s00410-016-1285-1

Korhonen, F. J., Clark, C., Brown, M., Bhattacharya, S., & Taylor, R. (2013). How long-lived is ultrahigh temperature (UHT) metamorphism? Constraints from zircon and monazite geochronology in the Eastern Ghats orogenic belt, India. *Precambrian Research*, 234, 322–350. https://doi.org/10.1016/j.precamres.2012.12.001

Korhonen, F. J., Clark, C., Brown, M., & Taylor, R. J. M. (2014). Taking the temperature of Earth's hottest crust. *Earth and Planetary Science Letters*, 408, 341–354. https://doi.org/10.1016/j.epsl.2014.10.028

Korhonen, F. J., Saw, A. K., Clark, C., Brown, M., & Bhattacharya, S. (2011). New constraints on UHT metamorphism in the Eastern Ghats Province through the application of phase equilibria modelling and in situ geochronology. *Gondwana Research*, 20(4), 764–781. https://doi.org/10.1016/j.gr.2011.05.006

Kunz, B. E., Regis, D., & Engi, M. (2018). Zircon ages in granulite facies rocks: Decoupling from geochemistry above 850° C? *Contributions to Mineralogy and Petrology*, 173, 1–21.

Kylander-Clark, A. R. C., Hacker, B. R., & Cottle, J. M. (2013). Laser-ablation split-stream ICP petrochronology. *Chemical Geology*, 345, 99–112. https://doi.org/10.1016/j.chemgeo.2013.02.019

Luvizotto, G. L., Zack, T., Meyer, H. P., Ludwig, T., Triebold, S., Kronz, A., Münker, C., Stockli, D. F., Prowatke, S., Klemme, S., Jacob, D. E., & von Eynatten, H. (2009). Rutile crystals as potential trace element and isotope mineral standards for microanalysis. *Chemical Geology*, 261(3–4), 346–369. https://doi.org/10.1016/j.chemgeo.2008.04.012

Mottram, C. M., Warren, C. J., Regis, D., Roberts, N. M. W., Harris, N. B. W., Argles, T. W., & Parrish, R. R. (2014). Developing an inverted Barrovian sequence; insights from monazite petrochronology. *Earth and Planetary Science Letters*, 403, 418–431. https://doi.org/10.1016/j.epsl.2014.07.006

Paton, C., Hellstrom, J., Paul, B., Woodhead, J., & Hergt, J. (2011). Iolite: Freeware for the visualisation and processing of mass spectrometric data. *Journal of Analytical Atomic Spectrometry*, 26(12), 2508–2518. https://doi.org/10.1039/c1ja10172b

Paton, C., Woodhead, J. D., Hellstrom, J. C., Hergt, J. M., Greig, A., & Maas, R. (2010). Improved laser ablation U-Pb zircon geochronology through robust downhole fractionation correction. *Geochemistry, Geophysics, Geosystems*, 11(3), 1–36.

Pearce, N. J. G., Perkins, W. T., Westgate, J. A., Gorton, M. P., Jackson, S. E., Neal, C. R., & Chenery, S. P. (1997). A compilation of new and published major and trace element data for NIST SRM 610 and NIST SRM 612 glass reference materials. *Geostandards Newsletter*, *21*(1), 115–144. https://doi.org/10.1111/j.1751-908X.1997.tb00538.x

Rubatto, D., Chakraborty, S., & Dasgupta, S. (2013). Timescales of crustal melting in the higher Himalayan Crystallines (Sikkim, Eastern Himalaya) inferred from trace element-constrained monazite and zircon chronology. *Contributions to Mineralogy and Petrology*, *165*(2), 349–372. https://doi.org/10.1007/s00410-012-0812-y

Rubatto, D., Hermann, J., & Buick, I. S. (2006). Temperature and bulk composition control on the growth of monazite and zircon during low-pressure anatexis (Mount Stafford, Central Australia). *Journal of Petrology*, *47*(10), 1973–1996. https://doi.org/10.1093/petrology/egl033

Seydoux-Guillaume, A. M., Fougerouse, D., Laurent, A. T., Gardés, E., Reddy, S. M., & Saxey, D. W. (2019). Nanoscale resetting of the Th/Pb system in an isotopically-closed monazite grain: A combined atom probe and transmission electron microscopy study. *Geoscience Frontiers*, *10*(1), 65–76. https://doi.org/10.1016/j.gsf.2018.09.004

Seydoux-Guillaume, A. M., Goncalves, P., Wirth, R., & Deutsch, A. (2003). Transmission electron microscope study of polyphase and discordant monazites: Site-specific specimen preparation using the focused ion beam technique. *Geology*, *31*(11), 973–976. https://doi.org/10.1130/G19582.1

Shaffer, M., Hacker, B. R., Ratschbacher, L., & Kylander-Clark, A. R. C. (2017). Foundering triggered by the collision of India and Asia captured in xenoliths. *Tectonics*, *36*(10), 1913–1933. https://doi.org/10.1002/2017TC004704

Sheraton, J. W., Tingey, R. J., Black, L. P., Offe, L. A., & Ellis, D. J. (1987). *Geology of enderby land and western Kemp Land* (p. 223). Bureau of Mineral Resources, Bulletin-Australia.

Sláma, J., Košler, J., Condon, D. J., Crowley, J. L., Gerdes, A., Hanchar, J. M., Horstwood, M. S. A., Morris, G. A., Nasdala, L., Norberg, N., Schaltegger, U., Schoene, B., Tubrett, M. N., & Whitehouse, M. J. (2008). Plešovice zircon—A new natural reference material for U-Pb and Hf isotopic microanalysis. *Chemical Geology*, *249*(1–2), 1–35. https://doi.org/10.1016/j.chemgeo.2007.11.005

Smye, A. J., Marsh, J. H., Vermeesch, P., Garber, J. M., & Stockli, D. F. (2018). Applications and limitations of U-Pb thermochronology to middle and lower crustal thermal histories. *Chemical Geology*, *494*, 1–18. https://doi.org/10.1016/j.chemgeo.2018.07.003

Suzuki, S., Arima, M., Williams, I. S., Shiraishi, K., & Kagami, H. (2006). Thermal history of UHT metamorphism in the Napier Complex, East Antarctica: Insights from zircon, monazite, and garnet ages. *The Journal of Geology*, *114*(1), 65–84.

Taylor, R. J. M., Clark, C., Fitzsimons, I. C. W., Santosh, M., Hand, M., Evans, N., & McDonald, B. (2014). Post-peak, fluid-mediated modification of granulite facies zircon and monazite in the Trivandrum Block, southern India. *Contributions to Mineralogy and Petrology*, *168*(2), 1044. https://doi.org/10.1007/s00410-014-1044-0

Tomkins, H. S., Powell, R., & Ellis, D. J. (2007). The pressure dependence of the zirconium-in-rutile thermometer. *Journal of Metamorphic Geology*, *25*(6), 703–713. https://doi.org/10.1111/j.1525-1314.2007.00724.x

Turuani, M. J., Laurent, A. T., Seydoux-Guillaume, A. M., Fougerouse, D., Saxey, D., Reddy, S. M., Harley, S. L., Reynaud, S., & Rickard, W. D. A. (2022). Partial retention of radiogenic Pb in galena nanocrystals explains discordance in monazite from Napier Complex (Antarctica). *Earth and Planetary Science Letters*, *588*, 117567. https://doi.org/10.1016/j.epsl.2022.117567

Turuani, M. J., Seydoux-Guillaume, A. M., Laurent, A. T., Reddy, S. M., Harley, S. L., Fougerouse, D., Saxey, D., Gouy, S., de Parseval, P., Reynaud, S., & Rickard, W. (2023). Nanoscale features revealed by a multiscale characterisation of discordant monazite highlight mobility mechanisms of Th and Pb. *Contributions to Mineralogy and Petrology*, *178*(5), 31. https://doi.org/10.1007/s00410-023-02015-x

Varga, J., Raimondo, T., Daczko, N. R., & Adam, J. (2020). Experimental alteration of monazite in granitic melt: Variable U–Th–Pb and REE mobility during melt-mediated coupled dissolution-precipitation. *Chemical Geology*, *544*, 119602. https://doi.org/10.1016/j.chemgeo.2020.119602

Warren, C. J., Greenwood, L. V., Argles, T. W., Roberts, N. M. W., Parrish, R. R., & Harris, N. B. W. (2019). Garnet–monazite rare earth element relationships in sub-solidus metapelites: A case study from Bhutan. *Geological Society, London, Special Publications*, *478*(1), 145–166. https://doi.org/10.1144/SP478.1

Watson, E. B., & Harrison, T. M. (2005). Zircon thermometer reveals minimum melting conditions on earliest Earth. *Science*, *308*(5723), 841–844. https://doi.org/10.1126/science.1110873

Weinberg, R. F., Wolfram, L. C., Nebel, O., Hasalová, P., Závada, P., Kylander-Clark, A. R. C., & Becchio, R. (2020). Decoupled U-Pb date and chemical zonation of monazite in migmatites: The case for disturbance of isotopic systematics by coupled dissolution-reprecipitation. *Geochimica et Cosmochimica Acta*, *269*, 398–412. https://doi.org/10.1016/j.gca.2019.10.024

Weller, O. M., Jackson, S., Miller, W. G. R., St-Onge, M. R., & Rayner, N. (2020). Quantitative elemental mapping of granulite-facies monazite: Textural insights and implications for petrochronology. *Journal of Metamorphic Geology*, *38*(8), 853–880. https://doi.org/10.1111/jmg.12552

Whitney, D. L., & Evans, B. W. (2010). Abbreviations for names of rock-forming minerals. *American Mineralogist*, *95*(1), 185–187. https://doi.org/10.2138/am.2010.3371

Wiedenbeck, M., Alle, P., Corfu, F. Y., Griffin, W. L., Meier, M., Oberli, F. V., Quadt, A. V., Roddick, J. C., & Spiegel, W. (1995). Three natural zircon standards for U-Th-Pb, Lu-Hf trace element and REE analyses. *Geostandards Newsletter*, *19*, 1–24. https://doi.org/10.1111/j.1751-908X.1995.tb00147.x

Williams, M. L., Jercinovic, M. J., Harlov, D. E., Budzyn, B., & Hetherington, C. J. (2011). Resetting monazite ages during fluid-related alteration. *Chemical Geology*, *283*(3–4), 218–225. https://doi.org/10.1016/j.chemgeo.2011.01.019

Wolf, M. B., & London, D. (1994). Apatite dissolution into peraluminous haplogranitic melts: An experimental study of solubilities and mechanisms. *Geochimica et Cosmochimica Acta*, *58*, 4127–4145. https://doi.org/10.1016/0016-7037(94)90269-0

Yakymchuk, C. (2017). Behaviour of apatite during partial melting of metapelites and consequences for prograde suprasolidus

monazite growth. *Lithos*, *274-275*, 412–426. https://doi.org/10.1016/j.lithos.2017.01.009

Yakymchuk, C., & Brown, M. (2014). Behaviour of zircon and monazite during crustal melting. *Journal of the Geological Society of London*, *171*, 465–479. https://doi.org/10.1144/jgs2013-115

Yakymchuk, C., Clark, C., & White, R. W. (2017). Phase relations, reaction sequences and petrochronology. *Reviews in Mineralogy and Geochemistry*, *83*(1), 13–53. https://doi.org/10.2138/rmg.2017.83.2

Zack, T., Stockli, D. F., Luvizotto, G. L., Barth, M. G., Belousova, E., Wolfe, M. R., & Hinton, R. W. (2011). In situ U-Pb rutile dating by LA-ICP-MS: Pb-208 correction and prospects for geological applications. *Contributions to Mineralogy and Petrology*, *162*(3), 515–530. https://doi.org/10.1007/s00410-011-0609-4

SUPPORTING INFORMATION

Additional supporting information can be found online in the Supporting Information section at the end of this article.

Table S1. U-Pb and trace element LASS data for monazite from Dallwitz Nunatak.

Table S2. U-Pb and trace element LASS data for rutile from Dallwitz Nunatak.

Table S3. U-Pb and trace element LASS data for zircon from Dallwitz Nunatak.

Table S4. LA-ICP-MS data for garnet from Dallwitz Nunatak.

Table S5. Empirical, derived and UHT monazite/garnet partitioning coefficients used to construct Figure 10.